



**HAL**  
open science

## Hydrothermal and Magmatic System of a Volcanic Island Inferred From Magnetotellurics, Seismicity, Self-potential, and Thermal Image: An Example of Miyakejima (Japan)

Marceau Gresse, Makoto Uyeshima, Takao Koyama, Hideaki Hase, Koki Aizawa, Yusuke Yamaya, Yuichi Morita, Derek Weller, Tawat Rung-Arunwan, Takayuki Kaneko, et al.

### ► To cite this version:

Marceau Gresse, Makoto Uyeshima, Takao Koyama, Hideaki Hase, Koki Aizawa, et al.. Hydrothermal and Magmatic System of a Volcanic Island Inferred From Magnetotellurics, Seismicity, Self-potential, and Thermal Image: An Example of Miyakejima (Japan). *Journal of Geophysical Research: Solid Earth*, 2021, 126, 10.1029/2021JB022034 . insu-03712634

**HAL Id: insu-03712634**

**<https://insu.hal.science/insu-03712634>**

Submitted on 6 Aug 2022

**HAL** is a multi-disciplinary open access archive for the deposit and dissemination of scientific research documents, whether they are published or not. The documents may come from teaching and research institutions in France or abroad, or from public or private research centers.

L'archive ouverte pluridisciplinaire **HAL**, est destinée au dépôt et à la diffusion de documents scientifiques de niveau recherche, publiés ou non, émanant des établissements d'enseignement et de recherche français ou étrangers, des laboratoires publics ou privés.

# JGR Solid Earth

## RESEARCH ARTICLE

10.1029/2021JB022034

### Key Points:

- An elongated aquifer (<1 km depth) lies between a resistive unsaturated layer and a conductive clay cap
- A gas-rich reservoir (2–4.5 km depth) feeds the main fumarolic area
- Magmatic gases interact during their ascent with a 1.2-km-long water-rich region creating local steam explosions

### Supporting Information:

Supporting Information may be found in the online version of this article.

### Correspondence to:

M. Gresse,  
[marceau.gresse@gmail.com](mailto:marceau.gresse@gmail.com)

### Citation:

Gresse, M., Uyeshima, M., Koyama, T., Hase, H., Aizawa, K., Yamaya, Y., et al. (2021). Hydrothermal and magmatic system of a volcanic island inferred from magnetotellurics, seismicity, self-potential, and thermal image: An example of Miyakejima (Japan). *Journal of Geophysical Research: Solid Earth*, 126, e2021JB022034. <https://doi.org/10.1029/2021JB022034>

Received 9 MAR 2021

Accepted 19 MAY 2021

### Author Contributions:

**Conceptualization:** Marceau Gresse, Makoto Uyeshima, Takao Koyama

**Data curation:** Marceau Gresse, Makoto Uyeshima, Takao Koyama, Hideaki Hase

**Formal analysis:** Marceau Gresse, Makoto Uyeshima, Takao Koyama

**Funding acquisition:** Makoto Uyeshima

**Investigation:** Marceau Gresse, Makoto Uyeshima, Takao Koyama

**Methodology:** Marceau Gresse, Makoto Uyeshima, Takao Koyama, Maki Hata

**Project Administration:** Makoto Uyeshima, Yuichi Morita

**Resources:** Makoto Uyeshima, Takao Koyama, Hideaki Hase, Yusuke Yamaya, Hideki Ueda

## Hydrothermal and Magmatic System of a Volcanic Island Inferred From Magnetotellurics, Seismicity, Self-potential, and Thermal Image: An Example of Miyakejima (Japan)

Marceau Gresse<sup>1</sup> , Makoto Uyeshima<sup>1</sup> , Takao Koyama<sup>1</sup>, Hideaki Hase<sup>2</sup>, Koki Aizawa<sup>3</sup>, Yusuke Yamaya<sup>4</sup> , Yuichi Morita<sup>1</sup>, Derek Weller<sup>1</sup>, Tawat Rung-Arunwan<sup>5</sup> , Takayuki Kaneko<sup>1</sup>, Yoichi Sasai<sup>6</sup>, Jacques Zlotnicki<sup>7</sup>, Tsuneo Ishido<sup>8</sup>, Hideki Ueda<sup>9</sup>, and Maki Hata<sup>1</sup> 

<sup>1</sup>Earthquake Research Institute, The University of Tokyo, Tokyo, Japan, <sup>2</sup>Geothermal Energy Research & Development Co., Ltd., Tokyo, Japan, <sup>3</sup>Institute of Seismology and Volcanology, Faculty of Science, Kyushu University, Fukuoka, Japan, <sup>4</sup>Renewable Energy Research Center, National Institute of Advanced Industrial Science and Technology (AIST), Koriyama, Japan, <sup>5</sup>Curl-E Geophysics Co., Ltd., Bangkok, Thailand, <sup>6</sup>Earthquake Prediction Research Center, Tokai University, Shizuoka, Japan, <sup>7</sup>CNRS, OPGC-UMR6524, Aubi re, France, <sup>8</sup>Geological Survey of Japan, National Institute of Advanced Industrial Science and Technology (AIST), Tsukuba, Japan, <sup>9</sup>National Research Institute for Earth Science and Disaster Resilience (NIED), Tsukuba, Japan

**Abstract** Phreatic and phreatomagmatic eruptions represent some of the greatest hazards occurring on volcanoes. They result from complex interactions at a depth between rock, water, and magmatic fluids. Understanding and assessing such processes remain a challenging task, notably because a large-scale characterization of volcanic edifices is often lacking. Here we focused on Miyakejima Island, an inhabited 8-km-wide stratovolcano with regular phreatomagmatic activity. We imaged its plumbing system through a combination of four geophysical techniques: magnetotellurics, seismicity, self-potential, and thermal image. We thus propose the first comprehensive interpretation of the volcanic island in terms of rock properties, temperature, fluid content, and fluid flow. We identify a shallow aquifer lying above a clay cap (<1 km depth) and reveal its relation with magmatic-tectonic features and past eruptive activity. At greater depths (2–4.5 km), we infer a seismogenic resistive region interpreted as a magmatic gas-rich reservoir ( $\geq 370^\circ\text{C}$ ). From this reservoir, gases rise through a fractured conduit before being released in the fumarolic area at  $\sim 180^\circ\text{C}$ . During their ascent, these hot fluids cross a  $\sim 1.2$ -km-long liquid-dominated zone causing local steam explosions. Such magmatic-hydrothermal interaction elucidates (i) the origin of the long-period seismic events and (ii) the mixing mechanism between magmatic and hydrothermal fluids, which was previously observed in the geochemical signature of fumaroles. Our results demonstrate that combining multidisciplinary large-scale methods is a relevant approach to better understand volcanic systems, with implications for monitoring strategies.

## 1. Introduction

Active hydrothermal systems develop during repose periods of volcanoes within the first kilometers of their edifices when ascending hot magmatic fluids (liquid or gas) encounter meteoric water recharge and/or seawater. Free convection and forced circulation occur, leading to surface manifestations such as fumaroles and hot springs.

Intensive volcanic hazards are associated with pervasive hydrothermal systems. Phreatic and phreatomagmatic eruptions represent the most common hazards occurring when hot magmatic fluids or magma are injected into a pre-existing hydrothermal system (Heiken & Wohletz, 1987; Stix, 2018). Pore-water is flashed creating an overpressure until the potential rupture of host-rock, leading to a sudden explosive eruption (e.g., Mannen et al., 2019; Yamaoka et al., 2016). Other hydrothermal-related hazards exist without necessarily involving magmatic origin. Indeed, long-term host-rock interactions between heat, water, and magmatic fluids lead to numerous modifications of the physical-chemical properties of host rocks and fluids. Percolation of hot and acidic fluids ( $< 400^\circ\text{C}$ ) dissolves host-rock primary minerals and precipitates low-permeability clay minerals (Pirajno, 2008). Such alteration products create a barrier to the flow of fluids (called

**Software:** Marceau Gresse, Makoto Uyeshima, Takao Koyama, Tawat Rung-Arunwan  
**Supervision:** Makoto Uyeshima, Takao Koyama  
**Validation:** Marceau Gresse, Makoto Uyeshima, Takao Koyama  
**Visualization:** Marceau Gresse  
**Writing – original draft:** Marceau Gresse, Makoto Uyeshima, Takao Koyama  
**Writing – review & editing:** Marceau Gresse, Makoto Uyeshima, Takao Koyama, Koki Aizawa, Derek Weller, Jacques Zlotnicki

cap rock) which can locally increase the pore-fluid pressure. If the pressure significantly exceeds that of the internal edifice, a hydrothermal explosion may occur (Browne & Lawless, 2001; Hedenquist & Henley, 1985). The combination of low mechanical properties of altered deposits in conjunction with fluid-pore pressurization can enhance flank instability, and may ultimately cause tsunamigenic edifice collapse and lateral blast explosions (e.g., López & Williams, 1993; Siebert et al., 1987).

Numerical modeling applied on hydrothermal systems have been widely developed in recent decades to describe fluid circulation (e.g., Aizawa et al., 2009; Ingebritsen et al., 2010; Ishido, 2004), and to study changes in subsoil properties (e.g., temperature, pressure, fluid-phase), in response to hydrogeological or magmatic perturbations (e.g., Ball et al., 2018; Chiodini et al., 2016; Hurwitz et al., 2003; Petrillo et al., 2019; Reid, 2004; Scott, 2020). These simulations showed a large influence of geological, tectonic, and boundary conditions settings (e.g., topography, rainfall) on the resulting hydrothermal structure. Hence, incorporating such information into models is a critical point to reduce their uncertainties, and enhance the comprehension of hydrothermal dynamics on volcanoes.

Subsoil characterization of magmatic-hydrothermal systems is classically obtained by measuring the electrical resistivity of rocks, due to its high sensitivity to fluid content, ionic charge of the pore water, temperature, and clay minerals (e.g., Roberts et al., 2001; Waff & Weill, 1975). Magnetotellurics (MT) is a geophysical method used to retrieve deep electrical resistivity distribution of volcanic edifices (e.g., Hata et al., 2018; Ogawa et al., 2014), while audio-magnetotellurics, time domain electromagnetic, and direct-current resistivity techniques are employed to investigate shallower regions (e.g., Dumont et al., 2019; Hogg et al., 2017; Kanda et al., 2019; Minami et al., 2018; Revil et al., 2010; Rosas-Carbalajal et al., 2016). When joined with seismic hypocenter locations (e.g., long-period events, see Text S1), electrical resistivity models can reveal magmatic-hydrothermal fluid paths and interactions (e.g., Hill et al., 2009; Matsunaga et al., 2020; Peacock et al., 2016; Usui et al., 2016). In addition, subaerial mappings including self-potential (Text S2), soil temperature, and CO<sub>2</sub> flux are often used to delineate shallow fluid circulation, and thus better interpret electrical resistivity models (e.g., Byrdina et al., 2014; Finizola et al., 2009; Gresse et al., 2017). In general, the upper part of a conductive hydrothermal plume is correlated with positive self-potential, thermal, and degassing anomalies (e.g., Aizawa, 2004; Revil et al., 2008).

Despite considerable progress to better understand volcanic edifices over the last century, fatal recent volcanic hazards (e.g., eruption of Mt Ontake in 2014 and White Island in 2019) originating from magmatic-hydrothermal interactions have outlined that their assessment remains limited. One of the reasons explaining this gap comes from the incomplete knowledge of volcanic structures at a large scale. Indeed, most studies using electrical resistivity methods only image shallow hydrothermal zones (<2 km depth) or deep magmatic structures (>5 km depth). Consequently, the complete subsoil range of magmatic-hydrothermal systems is often missing. Broadband MT, applied in the last ~3 decades, appears as one of the most capable methods to fill this gap, due to its sensitivity to both shallow and deep conductivity structures (e.g., Aizawa et al., 2004; Bedrosian et al., 2018; Heise et al., 2016; Hill et al., 2009; Piña-Varas et al., 2015). However, MT studies rarely provide sufficient attention to characterizing the nature of electrical resistivity, partly because additional subsoil-subsurface information is often incomplete or absent.

In this study, we focus on Miyakejima volcano, an 8-km wide island in the Pacific Ocean for the following reasons. First, this volcano has a short eruptive cycle (~20 years) with an extensive hydrothermal system posing a significant threat to the local population (4,000 residents in 2000). Second, the small size of the island facilitates the spatial coverage and the collection of data during fieldwork. Finally, Miyakejima has been indeed widely studied by geophysical methods, especially in terms of temporal variation of electrical resistivity (Zlotnicki et al., 2003), seismicity (e.g., Kobayashi et al., 2012; Uhira et al., 2005), geomagnetic (e.g., Sasai et al., 1997), self-potential (e.g., Kuwano et al., 2015; Sasai et al., 1997), GNSS (e.g., Munekane et al., 2016), synthetic aperture radar [e.g., Ozawa and Ueda, 2011], and gravity signals [e.g., Furuya et al., 2003]. However, a large-scale deterministic image of its structure remains lacking, which makes it difficult to properly understand and assess the role of its hydrothermal system involved in past phreato-magmatic eruptions. In addition, the Miyakejima plumbing system underwent significant modification during the 2000 A.D. eruption. Thus its future eruptive dynamics are likely to change, and it requires further evaluation.

We present here the first general image of Miyakejima's plumbing system down to 4.5 km depth, inferred from broadband MT, seismic hypocenters distribution, together with subaerial mappings: self-potential, and infrared thermal image. We propose a coherent interpretation of the volcanic edifice in terms of rock properties, temperature, fluid content, and fluid flow, allowing us to precisely characterize magmatic-hydrothermal interactions.

## 2. Geological Settings

Miyakejima is a basaltic-andesitic stratovolcano located in the Pacific Ocean, 180 km to the south of Tokyo in the Izu-Bonin volcanic arc (Figure 1a). The volcanic edifice rises from the seafloor of 500 m below sea level (bsl), and stands at 775 m above sea level (asl). The island has a sub-circular shape with a diameter of ~8 km with an area extent of 55 km<sup>2</sup>.

The formation of Miyakejima subaerial edifice can be divided into three periods, both ended by the formation of a new caldera (Tsukui & Suzuki, 1998; Tsukui et al., 2001):

- 1) The pre-Kuwanokitaira caldera period (>10 ka). Miyakejima oldest deposits (i.e. pyroclastic rocks and lavas) are observed on the western side of the island (Figure 1c, red layers). This stage ended with the creation of the Kuwanokitaira caldera (~4.5 km across), which may be associated with a phreatomagmatic eruption (Geshi et al., 2019).
- 2) The pre-Hatchodaira caldera period (~10–2.7 ka). After ~3 ka of repose period, volcanic activity resumed with the eruption of lava flows, scoria, and pyroclastic deposits that infilled the Kuwanokitaira caldera and formed a new stratocone (Figure 1c, brown layers). Finally, a second major collapse event generated the Hatchodaira caldera, 2 km across (Geshi & Oikawa, 2016).
- 3) The post-Hatchodaira caldera period (2.7 ka–2000 A.D.). Volcanic activity occurred within the Hatchodaira caldera, and formed a central stratocone (Mt. Oyama) composed of lava and scoria. However, most events erupted outside the caldera, along fissure systems-oriented in an SW–NE direction that is roughly perpendicular to the maximal regional compressive stress (Geshi & Oikawa, 2016). In several episodes, dikes encountered aquifers leading to phreatomagmatic eruptions (e.g., Furumio maar and Suoana-Kazahaya maars, Figure 1c). After regular eruptions occurring every ~20 years (1940, 1962, 1983, Figure S1), the last event took place in A.D. 2000. Volcanic activity was initiated by a minor submarine eruption (Kaneko et al., 2005), and a lateral dike migration toward Kozushima Island (Murase et al., 2006; Uhira et al., 2005) (Figure S2a). These events were simultaneously followed by an asymmetric collapse of the stratocone (Furuya et al., 2003; Geshi, 2009), creating the 2000 A.D. caldera (1.7 km across, and ~500 m deep, Figures 1b and 1c). Concurrently, deep-seated basaltic magma rose to shallow levels, and several phreatomagmatic eruptions occurred within the new caldera (Nakada et al., 2005; Saito et al., 2005). Finally, an intense degassing activity (up to ~400 kt of H<sub>2</sub>O, ~50 kt of SO<sub>2</sub> and ~26 kt of CO<sub>2</sub> per day) started in the caldera through the newly-created fumarolic region, and progressively decreased over the following decades (Kazahaya et al., 2004; Matsushima, 2005; Shinohara et al., 2017) (Figures 1b and S3a).

According to geochemical studies, eruptions at Miyakejima were historically supplied by two magmatic reservoirs (Amma-Miyasaka and Nakagawa, 2003; Yokoyama et al., 2003): a deep-seated basaltic chamber at 7–10 km bsl (SiO<sub>2</sub> = 48–52 wt %), and a shallow andesitic chamber at 2–5 km bsl (SiO<sub>2</sub> = 52–63 wt %). While most eruptions originated from a mixture of these two magmatic sources, a few recent events only involved magmas derived from the shallow andesitic reservoir (1835, 1962, 1983). However in 2000 A.D., analysis of eruptive deposits and gas composition indicates that the deep basaltic magma has erupted independently for the first time in at least 600 years (Amma-Miyasaka & Nakagawa, 2003; Geshi & Shinohara, 2010; Saito et al., 2010; Shinohara et al., 2017). Indeed, the shallow reservoir inferred in the SW part of the island (Figure 1c), is assumed to have been partially drained by the submarine eruption and the subsequent dike propagation toward Kozushima Island (Nishimura et al., 2001; Ueda et al., 2005) (Figure S2a). Recent geodesic and seismicity observations indicate however a residual or renewed activity at the location of the ancient andesitic reservoir (Morita & Ohminato, 2020).

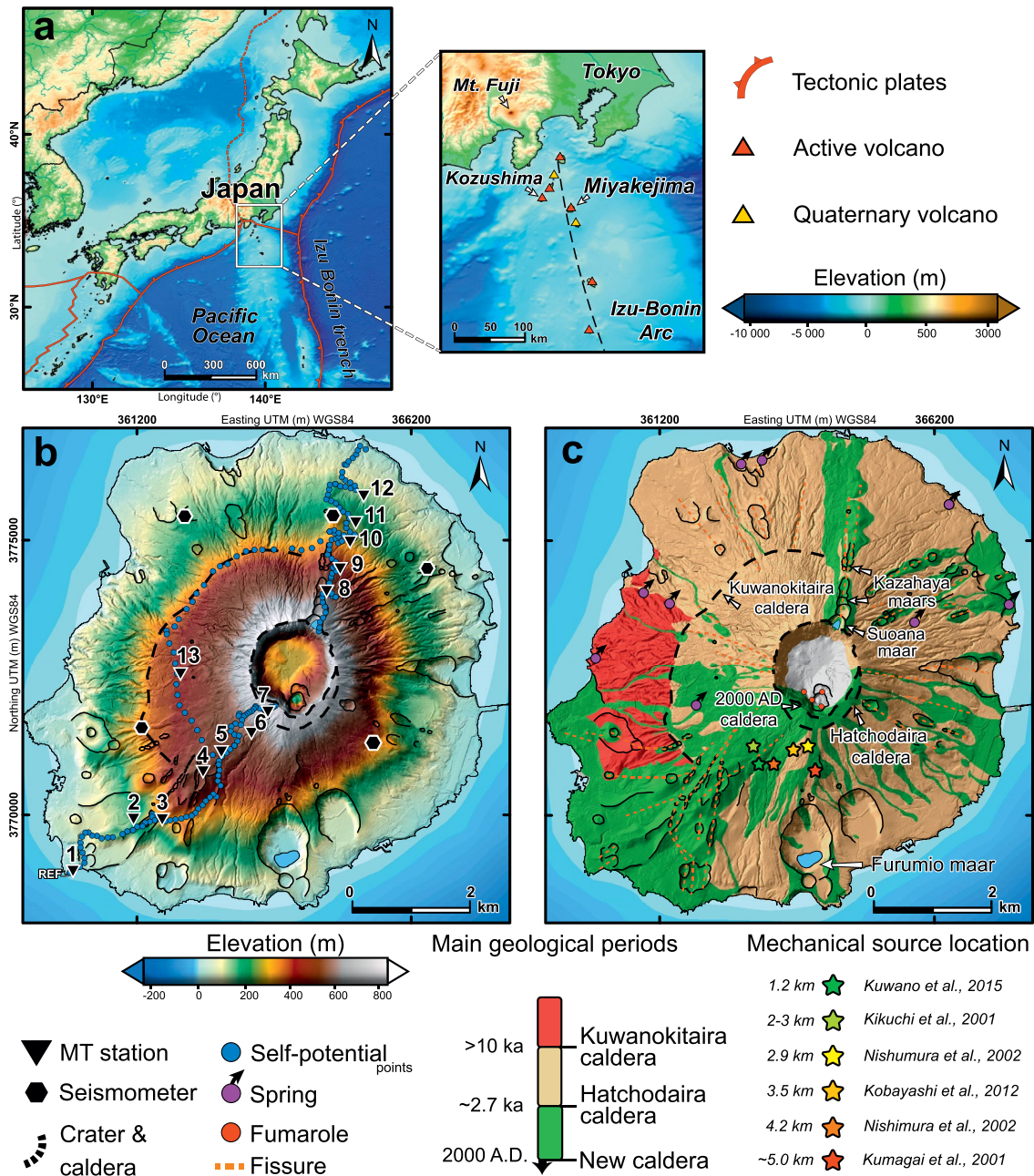


**Figure 1.** Miyakejima volcano (Japan) and its structural-geological context. (a) Overview of the Japanese archipelago and the Izu-Bonin volcanic arc. (b) Locations of magnetotelluric stations (black triangles), broadband seismometers (black hexagons), and self-potential measurements (blue points), (c) Simplified geological map overlain with topography showing the three main volcanic activity periods, together with fumaroles and springs (red and purple points, respectively). Colored stars indicate mechanical sources and depth associated to the shallow magmatic chamber inferred by several studies: Kuwano et al. [2015] from transient self-potential signal, Nishimura et al. [2002] from GPS data, Kobayashi et al. [2012] from velocity waveforms inversion using very-long-period events, Kumagai et al. [2001] and Kikuchi et al. [2001] from very long period seismic pulse. Maps were created using Esri ArcGIS 10.3 software (<http://www.esri.com>) with free digital elevation models: upper panel used the ASTER GDEM land model (<https://asterweb.jpl.nasa.gov/gdem.asp>) and the GEBCO bathymetry model (<https://download.gebco.net/>); bottom panels topography was obtained with the 5-m resolution digital elevation model of Miyakejima from the Geospatial Information Authority of Japan (<https://www.gsi.go.jp/kiban>). The geological map of Miyakejima used the free geographic information system database published by Tsukui et al. [2005], and was complemented with springs location from Sato et al. [2006].

### 3. Material and Methods

#### 3.1. Magnetotellurics

##### 3.1.1. Method

The MT method determines the subsurface electrical resistivity  $\rho$  ( $\Omega\cdot\text{m}$ ) (or its inverse, electrical conductivity  $\sigma$  in  $\text{S}\cdot\text{m}^{-1}$ ) by measuring, on Earth's surface, natural variations of electric and magnetic fields induced by remote natural sources (e.g., solar wind, lightning). Two types of complex transfer functions can be obtained from the frequency-domain ratios of these time series. First, the second-order impedance tensor  $\mathbf{Z}$  ( $\text{mV}\cdot\text{km}^{-1}\cdot\text{nT}^{-1}$ ) represents the ratio of electric field  $\mathbf{E}$  ( $\text{mV}\cdot\text{km}^{-1}$ ) and magnetic fields  $\mathbf{B}$  (nT) components at a given frequency  $f$  (Hz), expressed as:

$$\begin{pmatrix} E_x(f) \\ E_y(f) \end{pmatrix} = \begin{pmatrix} Z_{xx}(f) & Z_{xy}(f) \\ Z_{yx}(f) & Z_{yy}(f) \end{pmatrix} \begin{pmatrix} B_x(f) \\ B_y(f) \end{pmatrix}, \quad (1)$$

And second, the geomagnetic transfer functions  $\mathbf{T}$  (dimensionless) indicates the ratio of the vertical magnetic field to the horizontal magnetic field and is given by:

$$B_z(f) = \begin{pmatrix} T_x(f) & T_y(f) \end{pmatrix} \begin{pmatrix} B_x(f) \\ B_y(f) \end{pmatrix}, \quad (2)$$

where  $x, y, z$  subscripts denote components of northward, eastward, and downward directions, respectively. Each  $\mathbf{Z}$  component can be described with its magnitude by an apparent electrical resistivity  $\rho_a$ :

$$\rho_{a\,ij}(f) = \frac{|Z_{ij}(f)|^2}{5f}, \quad (3)$$

and by its phase  $\varphi$  ( $^\circ$ ):

$$\varphi_{ij}(f) = \arg(Z_{ij}(f)), \quad (4)$$

where  $i$  and  $j$  correspond to either  $x$  or  $y$  components.

In order to characterize MT transfer function data, induction vector (Parkinson, 1962) and phase tensor ellipse (Caldwell et al., 2004) can be represented for each frequency. The induction vector is expressed with the real part of  $\mathbf{T}$  as follows:

$$\vec{T}^{real}(f) = (-\text{Real } T_x(f), -\text{Real } T_y(f)). \quad (5)$$

The induction vector infers a lateral change in the electrical resistivity structure. It corresponds to the projection of the normal vector of a local plane of magnetic field variation on the horizontal  $xy$  plane, and it points toward high current concentration (i.e., conductive zones).

Phase tensor method is useful to investigate regional electrical resistivity structure because it is a galvanic distortion-free measure preserving phase information. This second order tensor  $\phi$  is expressed as:

$$\phi = \mathbf{X}^{-1}\mathbf{Y}, \quad (6)$$

with  $\mathbf{X}$  and  $\mathbf{Y}$  corresponding to the real and imaginary parts of  $\mathbf{Z}$ , respectively. This tensor can be graphically represented as an ellipse, where the major and minor axis ( $\phi_{\max}$  and  $\phi_{\min}$ ) indicate orientations of resistivity gradients. In order to provide information on the vertical resistivity gradient, the geometric mean of the phase tensor axes  $\phi_2$  ( $^\circ$ ) can be calculated as:

$$\phi_2 = \tan^{-1}\left(\sqrt{\phi_{\max}\phi_{\min}}\right), \quad (7)$$

Information on the regional resistivity asymmetry can be obtained by calculating the phase tensor skew angle  $\beta$  ( $^\circ$ ); a rotational invariant defined as:

$$\beta = \frac{1}{2} \tan^{-1} \left( \frac{sk(\phi)}{tr(\phi)} \right), \quad (8)$$

where  $sk(\phi)$  and  $tr(\phi)$  represent the skew and the trace of the phase tensor, respectively.

### 3.1.2. Acquisition, Processing, and Inversion

A Broadband MT survey was conducted at 13 sites in Miyakejima, between June and August 2012. Twelve MT stations were distributed along a SW–NE transect, while one station was located on the west part of the 2000 A.D. caldera (Figure 1b). Originally, one additional MT station was installed within the Furumio maar. Unfortunately, this station has been discarded from this study due to cultural noise, probably originating from a nearby water pumping station as reported by Arai (1978). Electric and magnetic time-series were recorded at 32 Hz and 1,024 Hz using Pb–PbCl electrodes ( $\sim 20$  m spacing) and broadband induction coil magnetometers MFS (Metronix), respectively. All-time series were collected using an ADU data logger (Metronix) and their timestamps were synchronized by GPS clocks.

MT transfer functions were calculated with the bounded influence, remote reference processing algorithm (BIRRP code) from Chave and Thomson (2003). For this purpose, two reference stations were employed. To process frequencies below 0.1 Hz, we used the 1 Hz geomagnetic time-series from the Kakioka Magnetic Observatory (free data portal <http://www.kakioka-jma.go.jp/en/>), located 250 km NNE of Miyakejima. In contrast, high frequencies were obtained with the 32 Hz and 1,024 Hz time-series from Sakurajima reference station, located 880 km SW of Miyakejima (Time-series details in Figure S4). In order to improve the transfer function quality, days where H-Alpha solar flare index activity (Özgüç et al., 2003) was null were removed from the processing (National Oceanic and Atmospheric Administration, <https://www.ngdc.noaa.gov>). Next, observed response functions  $\mathbf{Z}$  and  $\mathbf{T}$  were selected at 17 frequencies (0.0005–96 Hz), and outliers were removed (e.g., large error bars and anomalous deviations) from apparent resistivity and phase, and geomagnetic transfer functions (Figure 2). Finally, the resulting dataset consisted of 2,390 observations. Phase tensor ellipses and induction vectors are reported in Figure 3 with horizontal sections for four frequencies. In addition, all ellipses colored with  $\phi_2$  and  $\beta$  are presented in Figure S5.

The 3-D electrical resistivity model of Miyakejima was obtained by inverting MT response functions using the 3-D finite-difference inversion code WSINV3DMT (Siripunvaraporn & Egbert, 2009). The inverse problem was classically solved by minimizing the Occam's style function  $U(\mathbf{m}, \lambda)$ , using first-order isotropic spatial derivative with deterministic smoothing constraints:

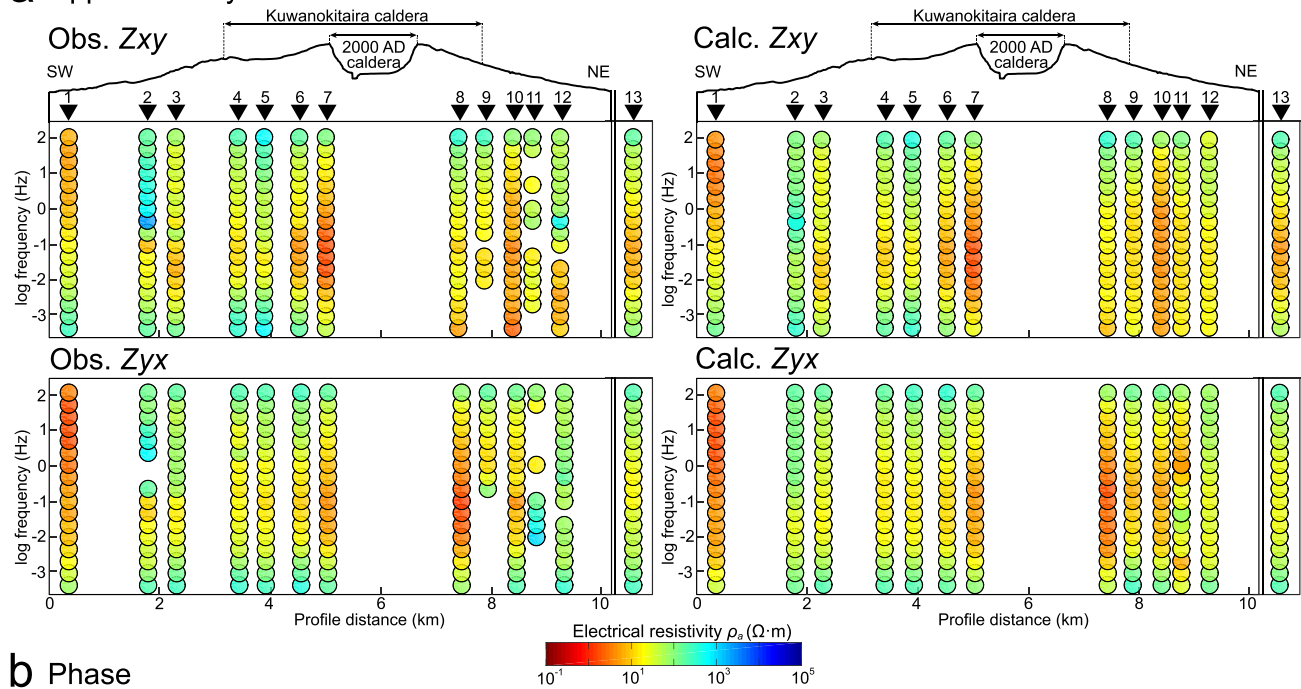
$$U(\mathbf{m}, \lambda) = (\mathbf{m} - \mathbf{m}_0)^T \mathbf{C}_m^{-1} (\mathbf{m} - \mathbf{m}_0) + \lambda^{-1} \left\{ (\mathbf{d} - \mathbf{F}[\mathbf{m}])^T \mathbf{C}_d^{-1} (\mathbf{d} - \mathbf{F}[\mathbf{m}]) - \chi^2 \right\}, \quad (9)$$

where,  $\mathbf{d}$  are the observed data of dimension  $\mathbf{N}$  (13 sites  $\times$  12 responses  $\times$  17 frequencies),  $\mathbf{m}$  and  $\mathbf{m}_0$  represent the logarithmic of the resistivity model  $\mathbf{m}$  and the prior resistivity model respectively,  $\mathbf{T}$  subscript is the transpose of the matrix,  $\mathbf{C}_m$  and  $\mathbf{C}_d$  are the model covariance matrix and the data covariance matrix, respectively,  $\mathbf{F}[\mathbf{m}]$  contains the synthetic data of the forward model response, and  $\lambda$  is the regularization parameter which is automatically updated at each iterative step to reduce  $U(\mathbf{m}, \lambda)$  (Siripunvaraporn et al., 2005). Inversion converges for a significant large  $\mathbf{N}$  when the normalized root-mean square (RMS) reaches 1:

$$RMS = \sqrt{\sum_{i=1}^N \mathbf{C}_{d_i}^{-1} \left( \frac{(\mathbf{d}_i - \mathbf{F}[\mathbf{m}]_i)^2}{N} \right)}. \quad (10)$$

The model space dimension was constructed with 362,952 elements ( $71 \times 71 \times 72$  cells) extending on a 200-km cube (Figure 4). In the central part of the domain, the mesh size was fixed to 200 m in the  $xy$  direction, and 30 m in the  $z$  direction. This discretization ensures accurate modeling of Miyakejima topography and

**a** App. resistivity



**b** Phase

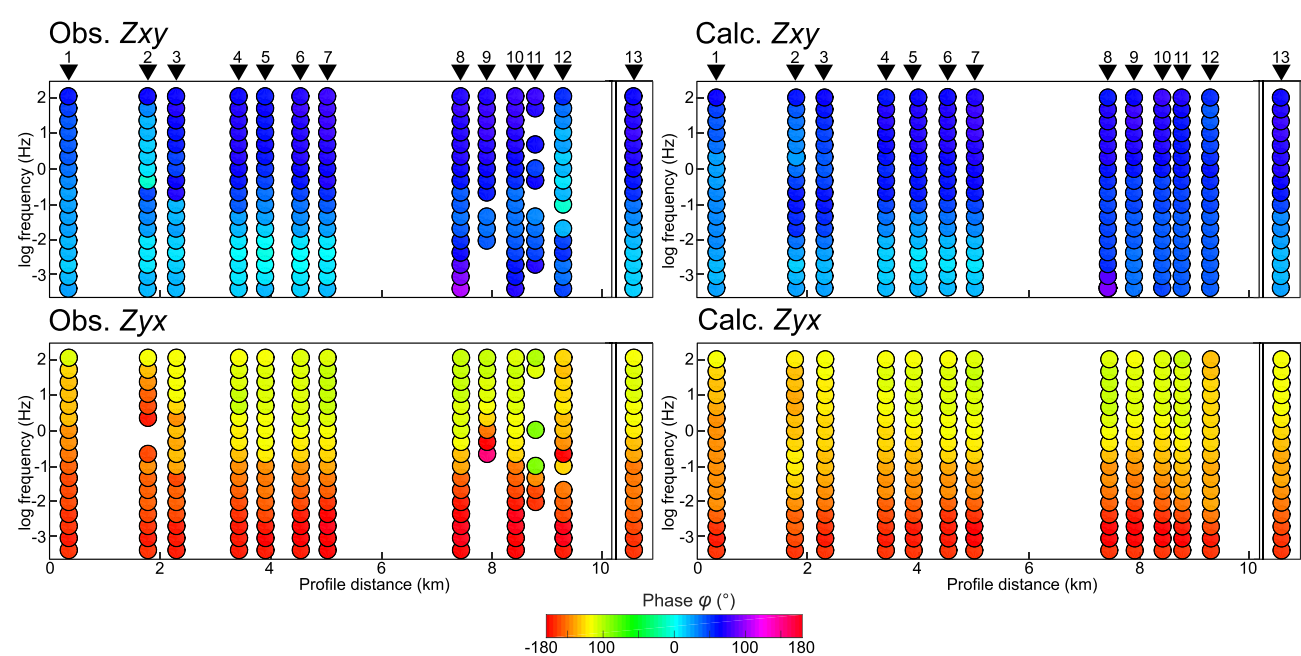


**Figure 2.** Comparisons of SW–NE pseudo-sections of apparent resistivity and phase between observed data (left panels) and calculated data (right panels) from the best fitting electrical resistivity model. (a) Observed and calculated apparent resistivity  $\rho_a$  ( $\Omega\text{-m}$ ) for  $Z_{xy}$  and  $Z_{yx}$  components. (b) Observed and calculated phase  $\varphi$  ( $^\circ$ ) for  $Z_{xy}$  and  $Z_{yx}$  components. Data are reported for 17 frequencies (0.0005–96 Hz). Discarded observed data were associated with large error bars to avoid any influence during the inversion. This figure was created using MATLAB software ([www.mathworks.com](http://www.mathworks.com)).

bathymetry while keeping a minimum of two cells between adjacent MT stations. The initial resistivity model was set to  $100 \Omega\text{-m}$  for land,  $10^7 \Omega\text{-m}$  for air, and  $0.2 \Omega\text{-m}$  for seawater (average value around Miyakejima latitude at 0–1,000 m depth, using the data set of ocean conductivity from Tyler et al. (2017)).

A two-steps inversion was performed by incrementally lowering the data error floor using a prior resistivity model. This approach mitigated local minimum effects with potentially unreliable structures, and helped to

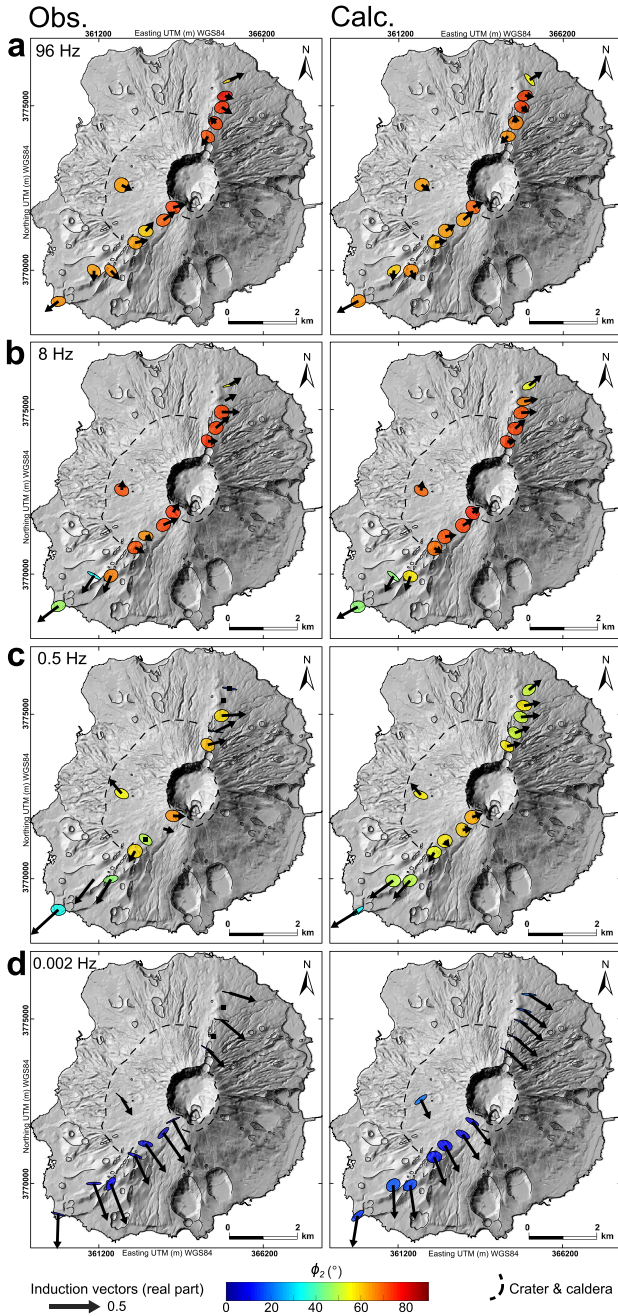


**Figure 3.** Phase tensor ellipses and induction vectors (Parkinson's convention) between observed data (left panels) and calculated data (right panels) from the best fitting electrical resistivity model. (a-d) Comparison of phase tensor ellipses and induction vectors at 96 Hz, 8 Hz, 0.5 Hz, and 0.002 Hz, respectively. Phase tensor ellipses are colored by the geometric mean  $\phi_2$  ( $^\circ$ ), and normalized by the maximum phase value  $\phi_{max}$ . Ellipses axis corresponds to the map orientation, and accounts for the magnetic declination at Miyakejima ( $-6.5^\circ$  in 2012). Black squares indicate missing phase tensor ellipses due to discarded observed data. Phase tensor ellipses and induction vectors are superimposed on the Miyakejima digital elevation model hillshade. The latter was created from the free 5-m resolution digital elevation model (reference in Figure 1).

accelerate the model convergence (Hata et al., 2017). The first inversion with four iterations was conducted assuming large error floors,  $Err_{Z,T}(f)$ , for response functions (Siripunvaraporn & Egbert, 2009):

$$|Err_Z(f)| = Err_{Z\%} \sqrt{|Z_{xy}(f) \times Z_{yx}(f)|}, \quad (11)$$

$$|Err_T(f)| = Err_{T\%} \sqrt{T_{zx}^2(f) + T_{zy}^2(f)}, \quad (12)$$

where  $Err_{Z\%}$  and  $Err_{T\%}$  were set to 20% and 30% respectively. Next, a second inversion with six iterations was carried out by taking the final resistivity distribution from the first step, as the initial and prior model. In this second step, the error floor was reduced to 15% and 20% for  $Err_{Z\%}$  and for  $Err_{T\%}$  respectively. After numerous tests with a careful inspection of results at each iteration, we decided to select the third iteration as the best model to prevent over fitting the data. Indeed, this iteration accurately matches the observations, while providing a plausible electrical resistivity structure (Figure 5). Hence, the final electrical resistivity model was obtained after a total of seven iterations, with the lowest normalized RMS value of our inversion procedure equal to 1.76 (Figure S6).

The WSINV3DMT code does not explicitly account for galvanic distortion produced by near-surface heterogeneities. In Miyakejima, no abrupt changes were observed in apparent resistivity in each site, compared with adjacent sites (Figure 2), which indicates that the static-shift effect remains limited.

In order to determine the sensitivity of the best fitting resistivity model, we followed an approach similar to Yoshimura et al. (2018). First, the absolute sensitivity matrix (Jacobian, L1 norm) of the best fitting resistivity model was extracted following Siripunvaraporn (2012) procedure:

$$\frac{1}{N} \sum_{i=1}^{i=N} |J(\text{Frequency, Site, Number of response})|, \quad (13)$$

where  $J = \partial_m F[m]$  is the sensitivity (Jacobian) matrix. Next, the sensitivity density distribution was calculated by dividing the absolute sensitivity values of each element by their volume. This step was important to reduce bias introduced by large elements in the absolute sensitivity matrix, which made it impossible to distinguish between constrained and unconstrained areas (Schwalenberg et al., 2002). Finally, histogram densities were plotted for the central and the external mesh domain (Figure S7). High sensitivity values were only located in the upper central domain near MT stations, while lower values were associated with background regions. This sharp contrast can be seen with the bimodal distributions intersecting at  $10^{-7}$ . We, therefore, set this value as the sensitivity limit of the final resistivity model.

In addition, forward models were carried out on each identified resistivity unit to check their robustness (Text S3).

### 3.2. Thermal Infrared Satellite Image

The surface temperature map of Miyakejima volcano was estimated from satellite remote sensing data. Two spectral radiance images were used due to their sensitivity to different temperature ranges. First, low-surface

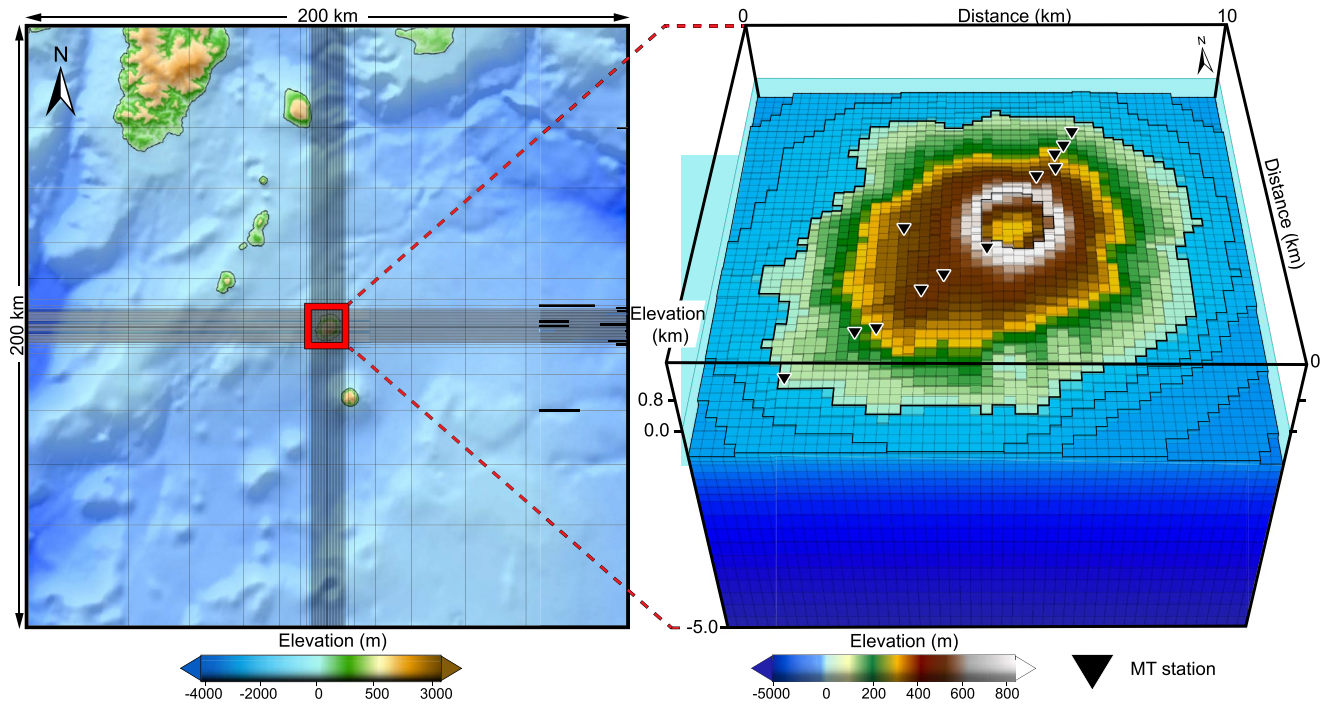


**Figure 4.** 3-D model space used for the inversion of the 2012 magnetotelluric data. Ocean is represented with the turquoise blue region on the right panel, while land is colored by elevation. Magnetotelluric stations are reported with black triangles. The 3-D mesh of Miyakejima volcano was constructed using the open-source VTK format (<https://vtk.org/>).

temperatures ( $-30$ – $+50^{\circ}\text{C}$ ) were recovered from the ASTER sensor, long-wave infrared (TIR) band 14 ( $10.95$ – $11.65\ \mu\text{m}$ ,  $90\text{-m}$  spatial resolution). Second, high thermal anomalies ( $+90$ – $+260^{\circ}\text{C}$ ) were obtained from the Landsat-7 ETM+ sensor, short-wave infrared (SWIR) band 7 ( $2.09$ – $2.350\ \mu\text{m}$ ,  $30\text{-m}$  resolution). To recover a representative thermal map associated with the 2012 MT survey, the closest ASTER and Landsat-7 cloud-free images were selected through the Earth Explorer USGS free data portal (<https://earthexplorer.usgs.gov/>). The ASTER TIR night-time image corresponded to January 31, 2012, 12:53 UTC. No night-time images were available for the Landsat-7 SWIR band, therefore, the closest day-time image used was on November 23, 2011, 01:10 UTC. For each spectral radiance image, land surface temperature  $t(\lambda)$  (K), was calculated through the inverse Planck Function (Planck, 1900):

$$t(\lambda) = \frac{c_2}{\lambda \ln \left( \frac{c_1 \lambda^{-5}}{R(\lambda)} + 1 \right)}, \quad (14)$$

where  $c_1 = 1.191042 \times 10^8$  ( $\text{W}\cdot\text{m}^{-2}\cdot\text{sr}^{-1}\cdot\mu\text{m}^4$ ) and  $c_2 = 1.42387752 \times 10^4$  ( $\text{K}\cdot\mu\text{m}$ ) are two constants, and  $\lambda$  ( $\mu\text{m}$ ) is the wavelength of the surface-emitted radiance  $R(\lambda)$  ( $\text{W}\cdot\text{m}^{-2}\cdot\text{sr}^{-1}\cdot\mu\text{m}^{-1}$ ). To retrieve  $R(\lambda)$ , corrections of calibrated at-satellite radiance  $R_m^*(\lambda)$  for atmospheric and emissivity effects were performed following Harris (2013) procedure for SWIR (day-time) and TIR (night-time) images, as follows:

$$R_{\text{SWIR}}(\lambda) = \frac{R_m^*(\lambda) - R_R(\lambda) - R_{\text{scat}}(\lambda)}{[\tau(\lambda) \varepsilon(\lambda)]}, \quad (15)$$

$$R_{\text{TIR}}(\lambda) = \frac{[R_{\text{in}}^*(\lambda) - R_{\text{U}}(\lambda)]}{[\tau(\lambda) \varepsilon(\lambda)]}, \quad (16)$$

where  $R_{\text{scat}}(\lambda)$  is the back-scattered solar radiance,  $R_{\text{U}}(\lambda)$  represents the atmosphere up-welling radiance, and  $\tau(\lambda)$  is the atmospheric transmittance (dimensionless). These parameters were estimated using the radiative transfer code MODTRAN assuming a model of mid-latitude winter atmosphere at an altitude of 300 m. The surface-reflected radiance  $R_{\text{R}}(\lambda)$  was obtained following the method described by Harris (2013), while surface emissivity  $\varepsilon(\lambda)$  (dimensionless) was retrieved using Sobrino et al. (1990) equation:

$$\varepsilon(\lambda) = \varepsilon_{\text{v}\lambda} P_{\text{v}} + \varepsilon_{\text{s}\lambda} (1 - P_{\text{v}}) + C_{\lambda}, \quad (17)$$

where  $\varepsilon_{\text{v}\lambda}$  and  $\varepsilon_{\text{s}\lambda}$  correspond to emissivity values of bare soil and full vegetation pixels set at 0.880 and 0.990, respectively. Emissivity map also accounted for surface water value set to 0.995 at Furumio crater lake (Figure S8a). The map of fractional vegetation cover  $P_{\text{v}}$  (Figure S8b) was determined through Carlson and Ripley (1997) formula:

$$P_{\text{v}} = \left( \frac{\text{NDVI} - \text{NDVI}_{\text{s}}}{\text{NDVI}_{\text{v}} - \text{NDVI}_{\text{s}}} \right)^2, \quad (18)$$

in which  $\text{NDVI}_{\text{s}}$  and  $\text{NDVI}_{\text{v}}$  are threshold values of the normalized difference vegetation index (NDVI), defined for bare soil and vegetation at 0.2 and 0.5, respectively (Walawender et al., 2012). The NDVI was calculated from Landsat-7 ETM+ image as:

$$\text{NDVI} = \frac{\text{Band4} - \text{Band3}}{\text{Band4} + \text{Band3}}, \quad (19)$$

In Equation 17, the last term  $C_{\lambda}$  corresponds to a surface roughness parameter, expressed as:

$$C_{\lambda} = (1 - \varepsilon_{\text{v}\lambda}) \varepsilon_{\text{s}\lambda} F' (1 - P_{\text{v}}), \quad (20)$$

where  $F'$  is a geometrical factor taken to a mean value of 0.55.

The thermal map obtained through inverse Planck Function (Equation 14) assumes homogeneous temperature for each pixel. However, when the pixel size is larger than a given thermal anomaly (e.g., small vent), an average temperature is recovered. To solve this effect of thermally mixed pixels, a dual band technique is often implemented (Dozier, 1981). Such a method could not be used here because the two radiance images have different resolutions and acquisition times. Nonetheless, similar temperature values were found between satellite-derived images and *in situ* measurements, indicating that the mixed pixel effect did not significantly influence the recovered thermal images (Text S4). Thus, we decided to combine temperatures from the two radiance images with the following procedure. First, low thermal anomalies ( $-30$ – $+50^{\circ}\text{C}$ ) were obtained for each pixel of the island with the corrected TIR image. Second, the corrected SWIR image mostly led to null radiance values, except in the fumarolic area. These null values indicated that there did not exist high temperatures ( $+90$ – $+260^{\circ}\text{C}$ ) and were excluded. Finally, the temperature map was retrieved by replacing, when available, TIR temperatures with SWIR ones at each pixel (Figures 5 and S8c).

### 3.3. Self-Potential Surveys and Processing

Electrical potential difference (voltage) was measured in Miyakejima using a high-impedance voltmeter (10 M $\Omega$ , sensitivity  $\pm 0.1$  mV) connected to a pair on non-polarizable Cu-CuSO<sub>4</sub> electrodes through an insulated copper wire. For each acquisition, a reference electrode was first placed in a small hole to ensure good contact with the soil. Next, the electrical potential was measured between the reference and distant electrodes. To complete long lines, several sub-profiles were necessary. Thus, every few hundred meters, the last measurement point of each sub-profile was transferred as a new sub-reference point. Electrical potential stability

was systematically checked with three repeated measures at each point. When a sub-profile was completed, the first pair of the electrode was remeasured in order to check for a shift in the self-potential and apply corrections if necessary.

Data acquisition was first performed with two long profiles along MT stations transect (SW–NE) (Figure 1 b). The southern profile was conducted on September 6–7, 2011, while the northern one was obtained from November 30 to 2 December 2, 2011. Distance between two adjacent sites was  $\sim 100$  m, and a total of 149 measurements were necessary to complete the two lines. When possible, self-potential was measured at MT stations. However, in some cases, a straight line between the two MT stations could not be maintained due to dense vegetation, and consequently, the survey line was curved. South and north profiles were connected using a third central profile carried out on June 14, 2012. The latter included 35 sites with a spacing of 200 m. Hence, the whole self-potential dataset was expressed with a unique reference point located at the southernmost site, and its value was set to 0 mV. Finally, 123 selected points (Figure S9) were presented together with the electrical resistivity cross-section in Figure 5.

It is worth noting that self-potential surveys were not carried out using closed loops technique, and thus a systematic error was introduced in the data (Grobbe & Barde-Cabusson, 2019; Revil & Jardani, 2013). However, this error remains small due to the low standard deviation recorded in most points ( $< 3$  mV). In addition, the temporal error introduced between the three profiles is assumed to be rather low, since (a) no significant variation of volcanic activity was observed at Miyakejima during the 2011–2012 interval (Figure S2c and S3), and (b) monthly precipitation was relatively constant during the period separating the north and south surveys ( $285 \pm 60$  mm  $\cdot$  month $^{-1}$ , Japan Meteorological Agency).

### 3.4. Hypocenters Localization and Classification

Miyakejima seismic activity is recorded since 1999 by five stations belonging to the network of the Japanese National Research Institute for Earth Science and Disaster Prevention (NIED) (Figures 1b and S2). Each station is composed of a two-component tiltmeter (1 Hz sampling rate) and a three-component short-period seismometer system (ABS-33 type, 100 Hz sampling rate) placed in a 100-m deep borehole. At the surface, stations include a three-component broadband seismometer (STS-2, 20 Hz sampling rate) and a GPS receiver. All the seismic data are continuously transmitted to the NIED Institute in Tsukuba (Japan).

Hypocenter coordinates were obtained after inverting arrival time data using a nonlinear maximum-likelihood algorithm developed by Hirata and Matsu'ura (1987). To better discriminate mechanisms behind earthquakes, hypocenters have been classified into three types depending on their waveform features and dominant frequencies (McNutt, 1996): long period (1–5 Hz), hybrid (3–9 Hz), and volcano-tectonic (5–15 Hz) (Text S1).

Following this classification, hypocenters were then selected for two periods. The first one started after the 2000 A.D. eruption and ended in August 2011 (Figure S2b), and it provided insight into events associated with the post-caldera collapse degassing activity (Figure S3). For this interval, only volcano-tectonic hypocenters above 5 km bsl and  $M_w > 0.8$  were selected (1,013 events). The second period extended from September 2011 to September 2012 (Figure S2c), since it covered the entire range of surveys presented in this article: magnetotellurics, self-potential, and thermal image mappings. All long-period hypocenters were picked (96 events), while hybrid ones were selected for  $M_w > -0.2$  (921 events), and volcano-tectonic ones were taken for  $M_w > 0.8$  (51 events). Selected hypocenters are presented together with the electrical resistivity model in Figure 5.

## 4. Results

### 4.1. Surface Temperature

The main thermal anomaly of Miyakejima (2011–2012) extends for  $\sim 60,000$  m $^2$  in the southern part of the 2000 A.D. caldera, with temperatures ranging from 20 to 181°C (Figures 5 and S8c). This area represents the only fumarolic zone within the volcanic island between 2000 and 2012. Except for this degassing region, no thermal anomalies are observed on the island with the thermal image.

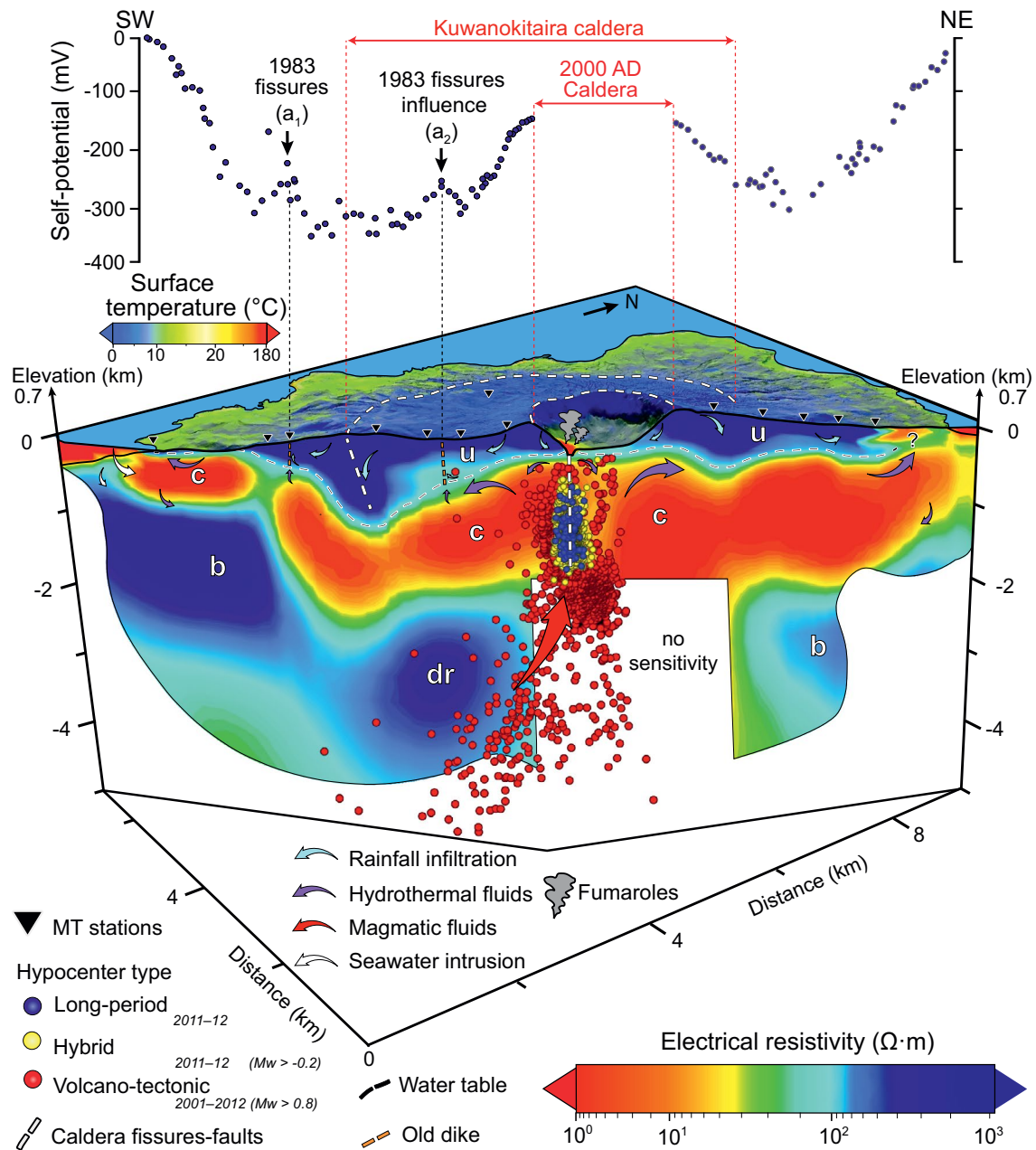


**Figure 5.** Vertical cross-section of Miyakejima volcano (SW–NE) showing the electrical resistivity model ( $\Omega\cdot\text{m}$ ) and selected hypocenters, overlain with surface temperature map ( $^{\circ}\text{C}$ ) and self-potential (mV). Principal units are ‘u’ = unsaturated deposits ( $130\text{--}2,200\ \Omega\cdot\text{m}$ ), ‘c’ = clay cap ( $2.5\text{--}30\ \Omega\cdot\text{m}$ ), ‘b’ = basement rocks ( $70\text{--}1,000\ \Omega\cdot\text{m}$ ), and ‘dr’ = deep resistor ( $200\text{--}500\ \Omega\cdot\text{m}$ ), see Section 4 and 5 for explanations. Fluid flows are represented with arrows: blue = rainfall infiltration, purple = hydrothermal fluids, red = magmatic fluids, and white = seawater intrusion. The estimated water table of the volcano (black dotted line) corresponds to the  $130\ \Omega\cdot\text{m}$  isovalue (Text S5). Self-potential points and hypocenters are projected along the two cross-sections aligned with the orientation of magnetotelluric stations (black triangles). Shallow seismicity in 2011–2012 is mainly composed of long-period and hybrid events (blue and yellow dots) located within the ‘c’ unit at 0–1.4 km bsl, revealing the volcano conduit. Deep seismicity (2001–2012) mostly consists of volcano-tectonic events (red dots) beneath the ‘c’ unit at 1.4–5 km bsl. Calderas are indicated by white dotted lines. Dikes associated with the 1983 eruption are reported by orange dotted lines as well as positive self-potential anomalies ( $a_1$  and  $a_2$ ). The electrical resistivity model is cut out at depth according to the threshold value of the sensitivity matrix (Figure S7) and sensitivity tests performed on each unit (Text S3).

Surface temperatures at the coastline ( $>8^{\circ}\text{C}$ ) reflect the ocean influence with higher temperature values than the ground surface in winter. Small temperature variations between the coastline and the summit ( $8^{\circ}\text{C}$  and  $0^{\circ}\text{C}$ , respectively) are mostly explained by the temperature gradient in the atmosphere ( $\sim 1^{\circ}\text{C}\cdot 100\text{ m}^{-1}$ ) originating from adiabatic decompression of air masses.

## 4.2. Self-Potential

The SW–NE self-potential profile (2011–2012) displays a total amplitude of 350 mV, with the highest values near south and north coastlines (Figure 5). The self-potential signal decreases with increasing elevation up to the Kuwanokitaira caldera. After this boundary, a central positive anomaly (+200 mV) is observed, with maximum values at the 2000 A.D. caldera rim. This classical ‘W’ shaped distribution (e.g., Ishido, 2004) is accompanied by two small-amplitude anomalies (+70 mV) in the southern part of the island. The southernmost anomaly ( $a_1$ ) coincides with the location of the 1983 fissure eruption, while the second one ( $a_2$ ) is  $\sim 200$  meters distant from the fissure (Figure S1).

## 4.3. Seismicity

Seismic activity following the 2000 A.D. eruption (2000–2007) was mostly composed of volcano-tectonic events (Figure S2b). These hypocenters extended on a  $\sim 3$ -km radius centered beneath the caldera floor, with an oblique structure down to  $\sim 5$  km bsl and a tilt angle of  $\sim 20^{\circ}$ . After 2007, deep volcano-tectonic signals progressively decreased while shallower hybrid events became dominant. In 2011–2012, Miyakejima hypocenters were distributed sub-vertically beneath the southern part of the 2000 A.D. caldera floor (Figure S2c). This seismicity displays coherent long-period events forming a channel-like structure from the fumarolic vent down to 1.2 km bsl, with a width of  $\sim 400$  m (Figure 5). A similar structure can be observed from hybrid and volcano-tectonic events although their distributions widen over  $\sim 1$ -km-large area, and extend to greater depths of 1.4 and 2 km bsl, respectively. Interestingly at 1.4–2 km bsl, volcano-tectonic events display a cluster with higher magnitudes ( $\sim 1.5$  km wide,  $M_w > 1$ , Figure S10).

## 4.4. Electrical Conductivity Model

### 4.4.1. Observed and Calculated Data

Apparent resistivity  $\rho_a$ , phase  $\varphi$  (Figure 2), and geometric mean phase  $\phi_2$  (Figure S5a) show overall a good agreement between observed and calculated impedance tensors  $\mathbf{Z}$ . Intermediate frequencies ( $\sim 0.01$ – $10$  Hz) reveal low apparent resistivities beneath the Kuwanokitaira caldera, highlighting the presence of a large conductive region. This conductive zone is also identified by the positive  $\phi_2$  gradient at high frequencies ( $\sim 10$ – $100$  Hz).

Induction vectors indicate a good consistency in terms of magnitude and direction between observed and calculated transfer functions  $\mathbf{T}$  (Figure 3). Above 1 Hz, vectors in the Kuwanokitaira caldera point toward the 2000 A.D. caldera, confirming the presence of a shallow conductive body in the central part of the island. As frequencies decrease ( $< 1$  Hz), all induction vectors progressively rotate toward the conductive ocean, with higher magnitudes near the coastline. For the lowest frequencies ( $< 0.001$  Hz), all vectors are oriented to the S–SE direction. An explanation for such direction is presented in Text S6.

Small skew angles ( $|\beta| < 1^{\circ}$ ) are mostly observed above 0.001 Hz in the central and southern MT sites (Figure S5b). For these frequencies, phase tensor ellipses are sub-circular (i.e.,  $\phi_{\max} \approx \phi_{\min}$ ), indicating that the regional resistivity structure can be considered 1-D or 2-D. On the contrary, in the northern MT sites at low frequencies ( $< 0.01$  Hz), high skew angle values ( $|\beta| > 2^{\circ}$ ) and elongated phase tensor ellipses ( $\phi_{\max} \neq \phi_{\min}$ ) reveal a complex 3-D structure. Such a pattern specifically affects the northernmost MT site for all frequencies. In this case, the resistivity model cannot properly reproduce the data, likely because of the lack of 3-D spatial coverage with MT sites.

#### 4.5. Description of the Main Units

The best fitting electrical resistivity model of Miyakejima volcano has a satisfactory depth of investigation down to 4.5 km bsl (Figure 5). Electrical resistivity values range from 2.5 to 2,200  $\Omega$ -m, and thus agree with the previous 1-D resistivity model obtained at Miyakejima by Zlotnicki et al. (2003) from audio-magnetotellurics soundings. This resistivity range is also consistent with several volcanic islands (e.g., Gailler et al., 2018; Piña-Varas et al., 2018; Pryet et al., 2012; Revil et al., 2011) and continental arc volcanoes (e.g., Aizawa et al., 2005; Heise et al., 2016).

The electrical resistivity model is classified into four units. The relevance of this selection in terms of rock properties and fluid flow is discussed in the following section and in Text S5. The main resistivity units identified are:

1. 'u' unit (unsaturated deposits): a high-resistive body (130–2,200  $\Omega$ -m) positioned at the surface of the volcano with a thickness up to 700 m. This long structure extends along the volcano's flanks up to the coastline but it is absent beneath the 2000 A.D. caldera. This unit is correlated with low surface temperature (<15°C).
2. 'c' unit (clay cap): a conductive layer (2.5–30  $\Omega$ -m) lying below the 'u' unit at 0–2 km bsl. This elongated layer rises near the 2000 A.D. caldera floor and at the coastline.
3. 'b' unit (basement rocks): a resistive body (70–1,000  $\Omega$ -m) in the southern and northern part of the island, extending gradually from the seabed down to 2.5 and 3.5 km bsl, respectively.
4. 'dr' unit (deep resistor): a resistive region (200–500  $\Omega$ -m) below the 'c' unit, at 2–4.5 km bsl, with an offset of ~1.5 km to the SW of the 2000 A.D. caldera.

The results of the sensitivity tests performed on each unit (Text S3) indicate that they are all reliable except at two locations. First, a deep conductor (2.5–30  $\Omega$ -m, 2–5 km bsl) beneath the 2000 A.D. caldera, which we have thus removed from the resistivity cross-section. Second, the northern basement unit: this unit is already mainly absent from the resistivity cross-section, and consequently we decided not to make an additional cut.

## 5. Discussion

### 5.1. Unsaturated Deposits and Water Table

In Miyakejima, a sharp resistivity contrast exists between the superficial high-resistive materials ('u' unit) and the underlying conductive ones ('c' unit). Such vertical variation is often observed on active volcanoes that include significant topography and meteoric recharge (e.g., Aizawa et al., 2005; Gailler et al., 2018; Piña-Varas et al., 2014; Revil et al., 2011; Rosas-Carbajal et al., 2016; Triahadini et al., 2019; Usui et al., 2016). This change in electrical resistivity is generally interpreted as a shift from unsaturated to water-saturated regime, delimiting the water table boundary of the volcano (e.g., Aizawa et al., 2009; Hurwitz et al., 2003).

In order to accurately understand the cause of the high-resistive 'u' unit in Miyakejima, we have calculated the theoretical electrical resistivity of fully unsaturated porous rock, and its transition to water-saturated conditions. To this purpose, we used Archie's Law and Waxman-Smiths equation (Waxman & Smits, 1968) accounting for Miyakejima's petrophysical rock properties and combined it with an empirical law to reduce the porosity at depth (Text S5). We assumed an average rock temperature of 15°C since no thermal anomalies were associated with the resistive 'u' unit (Figures 5 and S8c). The calculated range of the 'u' unit (130–2,145  $\Omega$ -m) shows an excellent agreement with the electrical resistivity model (130–2,200  $\Omega$ -m), thus explaining the nature of the resistive structure by an unsaturated layer. Therefore, the 130  $\Omega$ -m isovalue (water-saturated conditions) was used to define the apparent water table of the volcano. Near the coastline, the position of this aquifer is consistent with the presence of shallow wells and springs (Aoki et al., 1984; Arai et al., 1977; Sato et al., 2006). In the central part of the island, the deep position of the estimated water table (300–700 m below the ground surface) is also coherent by the absence of large springs and wells. Nevertheless, few cold springs with small discharge rate (0.1–10 L·min<sup>-1</sup>) observed by Sato et al. (2006) at 200–500 m asl, indicate the presence of minor perched aquifers lying above thin ash layers. These small and scattered aquifers have no visible effects on the large resistivity structure, suggesting a limited influence in the Miyakejima's hydrogeological cycle.

### 5.2. Clay Cap

The elongated conductive 'c' unit (2.5–30  $\Omega$ -m) lies below the water table and thus, belongs to the water-saturated zone (Figure 5). This structure is connected to the main fumarolic area, indicating significant fluid-rock alteration at depth. In Miyakejima, products of the 2000 A.D. eruption included wall rock fragments that were altered with up to 20% of smectite in a mass fraction (Yasuda et al., 2002).

To properly constrain the nature of the conductive 'c' unit, electrical resistivity was calculated for three water-saturated domains with different degrees of rock alteration and temperature (Text S5). First, an upper domain just beneath the water table, with a low alteration degree at 50°C including 4% of smectite in mass fraction. Second, a central altered domain at 200°C containing 20% of smectite. Third, a highly altered domain corresponding to the bottom region of the clay cap at 250°C with 4% of smectite. In this last case, the lower amount of smectite is defined to account for its transformation into chlorite and epidote (less conductive minerals) above 230°C (Árnason et al., 2010; Flóvenz et al., 2005). The calculated resistivities for the upper, central, and bottom domains of the 'c' unit are 2.6, 26, and 6  $\Omega$ -m, respectively. These three values match the 'c' unit range, indicating that its resistivities can be explained by different content of altered minerals, which is a temperature-controlled process. Therefore, we interpret this 'c' unit as a large clay cap zone, often identified on volcanoes and geothermal systems (e.g., Flóvenz et al., 2005; Hogg et al., 2017; Tsukamoto et al., 2018; Uchida, 2005; Yamaya et al., 2013).

Permeability of the clay cap generally reduces as the smectite content increases with temperature up to 200°C (e.g., Revil et al., 2019). Hence, the central (and most conductive) domain of the clay cap may act as a low-permeable boundary limiting fluid circulation. The local rupture of this layer, (due to a dike intrusion or the pressurization of underlying fluids) can transiently release a large amount of heat in the shallow hydrothermal system, which can generate a sudden explosive eruption (e.g., Mannen et al., 2021).

It is important to note that conductive clay caps can exist in geothermal regions with temperatures below 150–200°C, due to ancient or inactive sections of hydrothermal systems (e.g., Piña-Varas et al., 2018). Thus, clay caps do not always reflect the true temperature field of a system (e.g., Lévy et al., 2018). In Miyakejima, we believe this scenario is unlikely since it is a small-size and regularly active volcano, with persistent evidences of fluid circulation. This regular activity, mostly along the SW–NE fissure system, may also explain the consistent lateral and vertical extent of the clay cap. Indeed, the long-term host-rock alteration at a relatively constant temperature (~100–200°C) can produce a physico-chemical equilibrium between hydrothermal fluids and altered rocks (Pirajno, 2008). For these reasons, we propose that the clay cap resistivity can be used as a first-order approximation to (i) assess the upper thermal structure on small active volcanic edifices, and (ii) define the position of a low permeability layer above which a water-rich zone can be located.

### 5.3. Basement Rocks

The 'b' unit (70–1,000  $\Omega$ -m) near Miyakejima coastlines is not associated with any seismic activity in recent historical eruptions (Minakami, 1974; Ueda et al., 2005; Ueki et al., 1984). Such aseismic and resistive zones often lie on the edge of hydrothermal systems (e.g., Bertrand et al., 2013; Cordell et al., 2018; Heise et al., 2016; Hill et al., 2015; Samrock et al., 2018; Yamaya et al., 2017), and are usually interpreted as low-porous rocks without major thermal anomalies.

In order to understand the origin of the resistive 'b' unit in Miyakejima, electrical resistivity was calculated assuming a classic geothermal gradient for the oceanic crust and a reduction of porosity at depth (Text S5). The calculated resistivity range (66–490  $\Omega$ -m) shows a relatively good match with the model (70–1,000  $\Omega$ -m), except for a few high values. Hence, we suggest that the 'b' unit could represent a basement zone formed by old submarine volcanic materials that are possibly associated with low-permeabilities (e.g., Izquierdo, 2014; Join et al., 2005).

### 5.4. Magmatic Fluids Reservoir

Determining the characteristics of the resistive 'dr' unit (200–500  $\Omega$ -m) is a central point to understand the plumbing system of Miyakejima since it coincides with the location of several source mechanisms inferred during the 2000 A.D. eruption (Figure 1 and references therein). This resistive zone is also associated with

the deepest seismicity recorded on the volcano, which forms a channel-like structure connected to the fumarolic area (Figures 5, S2b, and S2c). The predominance of volcano-tectonic events down to  $\sim 5$  km depth suggests that the brittle regime dominates the upper part of the volcano (Ito, 1993). Thus, it implies that the average rock temperature of this region should range between that of the main vents ( $>350^\circ\text{C}$  in 2000–2006, Figure S3c), and that associated with the onset of the brittle-ductile transition ( $\sim 550 \pm 100^\circ\text{C}$  for basalt, after Violay et al. [2012]). Under these temperature and pressure conditions (hydrostatic regime), the porous phase is either dominated by superheated or supercritical fluids. Indeed, critical points of pure water and seawater range between  $373^\circ\text{C}$  at 220 bar and  $403^\circ\text{C}$  at 298 bar, respectively. On volcanoes and geothermal areas, the presence of steam, or supercritical water in porous media is known to increase electrical resistivity compared to a liquid water phase (e.g., Árnason et al., 2010; Gasperikova et al., 2015; Hersir et al., 2020; Piña-Varas et al., 2014; Soyer et al., 2018; Yamaya et al., 2013). Such field observations are also attested by numerous laboratory measurements (e.g., Klumbach & Keppler, 2020; Nono et al., 2020; Quist & Marshall, 1968; Roberts et al., 2001).

In Miyakejima, electrical resistivity calculations performed in Text S5 support that steam (or superheated water) can explain the high resistivity values of the 'dr' unit, while a liquid-dominated regime cannot. For this reason, we suggest that the 'dr' unit could represent a two-phase or supercritical fluid reservoir feeding the fumarolic area. We propose that this reservoir would have developed above the residual part of the shallow andesitic chamber, involved in Miyakejima eruptions since at least the 15th century (Amma-Miyasaka et al., 2005; Ushioda et al., 2018). Magmatic gases stored in this reservoir would have two origins: (i) a small portion linked to the long-term crystallization of the shallow andesitic body, and (ii) a large amount coming from intrusions of the deep basaltic source. A recent multiphase flow simulation performed by Scott et al. (2015) confirms that a gas-rich zone, similar to the 'dr' unit, can be formed above a shallow magmatic intrusion after several hundred years. Other fluid models reveal that the extent of such gas-dominated region can be controlled by permeability contrasts induced by a clay cap (Scott, 2020) or a self-sealing zone (Fournier, 2007; Weis, 2015).

Interestingly, a large conductor ( $<5 \Omega\cdot\text{m}$ ) associated with a magmatic body is not observed in the best fitting resistivity model. Its absence could indicate that the shallow magma chamber does not exist anymore, is distant from the MT sites, or is too small to be resolved with the MT spatial coverage (e.g., Lee et al., 2020; Piña-Varas et al., 2018).

### 5.5. Fluid-Flow Structure and Magmatic-Hydrothermal Interactions

A general fluid flow model of Miyakejima volcano is proposed here based on a joint interpretation of electrical resistivity and seismic signatures, together with subaerial boundary conditions (self-potential and thermal maps), and previous literature.

Magmatic fluids are released from a deep-seated basaltic source (7–10 km depth) and remain stored within the 'dr' reservoir (2–4.5 km depth) corresponding to the residual andesitic chamber. Some of these volatiles accumulate beneath the central part of the clay cap (1.4–2 km bsl), creating a large volcano-tectonic cluster (Figures 5 and S10). This seismic cluster could also represent the location of the upper 2000 A.D. basaltic intrusion inferred by Sasai et al. (2002) from magnetic field measurements. In either case, exsolved gases ascend in the fractured and permeable conduit formed after the caldera collapse, and their energy is partly transferred to the surrounding liquid-dominated region. At this interface, liquid water filling fractures can be heated above a threshold pressure, which causes transient crack openings (Ohminato, 2006). The resulting pressure drop in fractures generates violent vaporization of water (Matoza & Chouet, 2010). We suggest that this explosive phase change explains the long-period events, while the reverberation of shockwaves could be associated with hybrid signals. This seismicity likely unravels the  $\sim 1.2$  km-long geometry of the upper conduit. We propose that this mechanism is also responsible for the mixing between hydrothermal and magmatic fluids, as observed by Shinohara et al. (2017) with the increase of the  $\text{H}_2\text{O}/\text{SO}_2$  gas ratio after the 2000 A.D. eruption (Figure S3b).

The mixture of hydrothermal and magmatic fluids discharges at the fumarolic area and condenses at the near surface of the caldera floor. A 2-km-wide conductive plume is attested beneath the 2000 A.D. caldera by the positive self-potential anomaly detected from its rim. This fluid upwelling was already observed before

the last eruption by Sasai et al. (1997), although its dynamics have been likely modified due to the collapse of the Oyama stratocone.

Intense annual precipitation affects Miyakejima Island (2,950 mm·year<sup>-1</sup>, 1981–2010, Japan Meteorological Agency) due to extensive evaporation of the hot ocean, and sea-breeze convergence over coastal zones (Qian, 2008). A significant amount of such meteoric water (30–50%, after Machida & Lee [2008]) percolates downward through the soil until it reaches a water-saturated layer. Despite a large amount of recharge, the highly permeable deposits of Miyakejima (10<sup>-9</sup>–10<sup>-12</sup> m<sup>2</sup> after Arai [1978]) keep the main aquifer a few hundred meters below the surface. In addition to the main hydrothermal plume, two parameters locally affect the water table level of Miyakejima:

1. The Kuwanokitaira caldera. This structural boundary forms a highly-permeable path for rainfall infiltration. At the southern caldera limit, the water table level is lowered below the sea level, and it is associated with the minimum self-potential value. Such a “negative” water table is rare, but can locally exist on volcanic islands (e.g., Cabrera & Custodio, 2004; Jackson & Kauahikaua, 1987). On the contrary, in the northern region, the Kuwanokitaira caldera boundary stops 1 km west of the MT stations, which probably explains the absence of a deep unsaturated layer in this area.
2. The 1983 fissure eruption. The residual heat and fractures created by the 1983 dikes induce small-scale aquifer upwellings (Sasai et al., 1997). This assumption is supported at the south vent by a positive self-potential anomaly ( $a_1$ ) correlated with diffuse soil CO<sub>2</sub> degassing (Hernández et al., 2001). However, the water table upwelling cannot be imaged, likely because of the limited resolution of the resistivity model in this area. The second self-potential anomaly ( $a_2$ ), although slightly shifted from the vent (~200 m), reflects a moderate water-table upwelling observed by the resistivity image (Figure 5).

Groundwater formed by the mixture of meteoric recharge and hydrothermal fluids is mostly driven toward the ocean due to the water table gradient. The current and past positive self-potential anomalies (Nishida et al., 1996; Sasai et al., 1997), as well as hydrogeological studies (Aoki et al., 1984; Machida & Lee, 2008; Sato et al., 2006), confirm this general fluid circulation. Near the coastlines, groundwater mixes with marine water, as revealed by geochemical analysis of water and 1-D resistivity surveys (Aoki et al., 1984; Sato et al., 2006). Locally, groundwater is discharged either onshore with springs and hot springs, or offshore. It is also probable that a small amount of such water infiltrates the low permeable basement unit, forming a convective cell, as shown by Ishido (2004) with multiphase flow simulation.

Figure 6 summarizes these observations and our interpretation of the current Miyakejima plumbing system.

### 5.6. Implication for Hydrothermal-Related Hazards

Historical phreatomagmatic eruptions on Miyakejima (i.e., tuff cone, tuff ring, maar diatreme) mainly occurred near the coastline, at the summit, and in the upper segment of the Suoana-Kazahaya eruption (Figure S1). In these regions, the aquifer is shallow (<300 m depth) and large, thus a magmatic intrusion can potentially produce stress exceeding the confining pressure which leads to an explosive eruption.

Conversely, other regions are mainly characterized by fissure eruptions with lava flow and scoria emissions. These areas are characterized by either deep and wide aquifers (e.g., Kuwanokitaira caldera, 300–700 m depth), or shallow and thin aquifers (e.g., lower segment of Suoana-Kazahaya eruption). In both cases, it is likely that the over pressure resulting from the vaporization of the aquifer does not exceed the lithostatic pressure, and thus a magmatic intrusion ends with a non-explosive activity (Figure 6).

## 6. Conclusion

We have revealed the first large-scale image of the Miyakejima plumbing system (0–4.5 km depth) by combining four geophysical methods: magnetotellurics, seismicity, self-potential, and surface thermal image. The resulting data were jointly interpreted with a particular focus on understanding the significance of the electrical resistivity using Archie’s Law and Waxman-Smits equation. Thus, we proposed a coherent characterization of the main hydrothermal-magmatic structures in terms of rock properties, temperature, fluid content, and fluid flow.

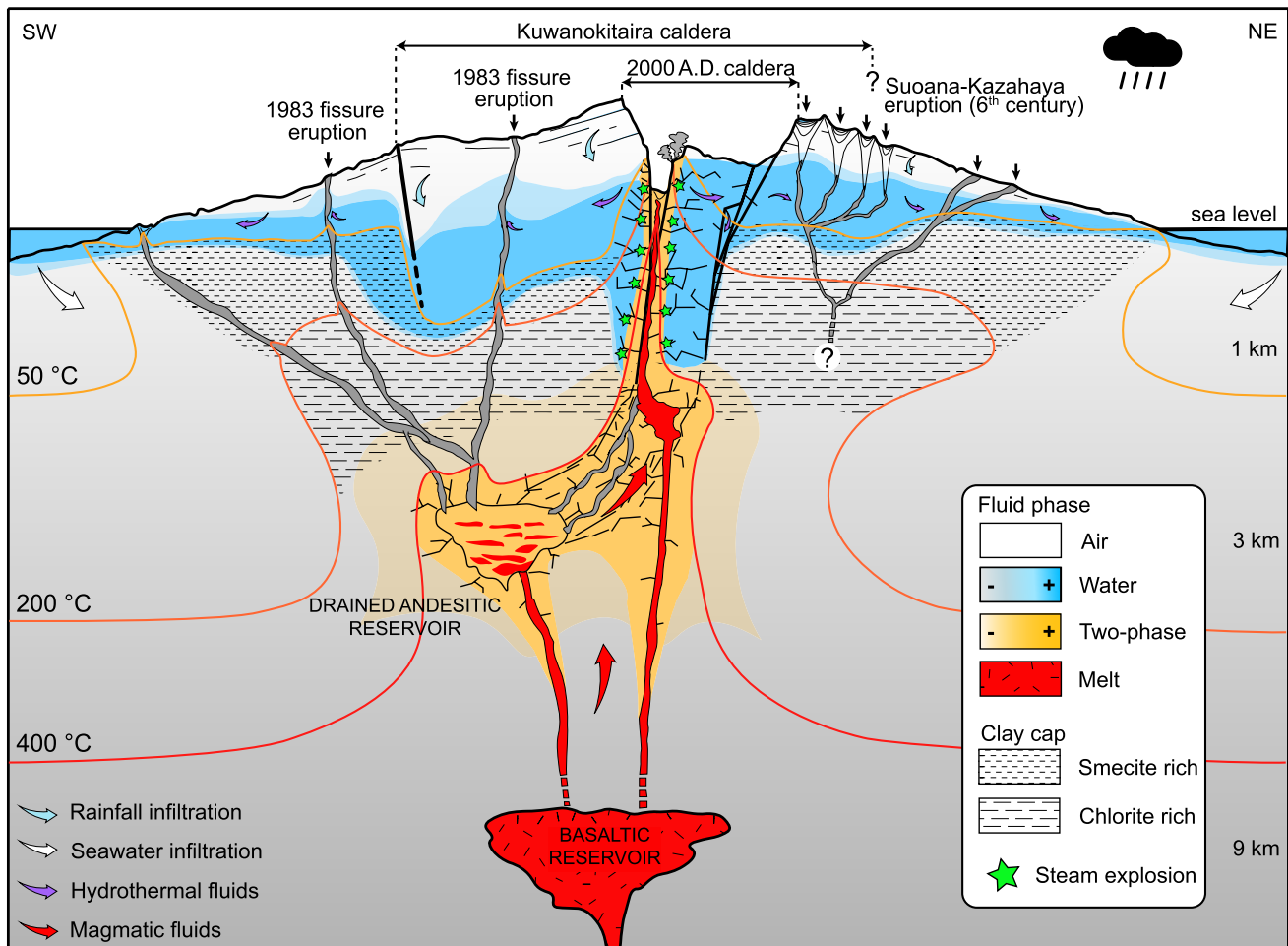


**Figure 6.** Interpretative scheme of Miyakejima plumbing system after the 2000 A.D. eruption. The partial drainage of the shallow andesitic reservoir (2.5–4.5 km bsl) due to the NW migration of dikes toward Kozushima Island (orthogonal to this cross-section), and the subsequent formation of the 2000 A.D. caldera have induced an expansion of a gas-rich region, trapped beneath a low-permeable clay cap. The aquifer position is controlled by the upper clay layer, and is influenced by recent volcanic activity (e.g., 1983 fissure eruption, west black arrows), and tectonic structures (e.g., Kuwanokitaira caldera). The location and the thickness of the aquifer affect the nature of the eruptive activity: explosive events are mainly located where a large aquifer reaches shallow regions (< 300 m depth, e.g., Suoana-Kazahaya eruption), while effusive activity occurs where the aquifer is deep (> 300 m depth) or thin. A water-rich region progressively developed in the fractured conduit formed by the 2000 A.D. caldera collapse. In this area, the heat originating from the degassing activity and the basaltic intrusion produces minor steam explosions (green stars) at the interface between gas and liquid-dominated regions. This magmatic-hydrothermal interaction induces the long-period seismicity signals down to 1.2 km bsl.

The estimated water table position of the island (0–700 m depth) reflects the complex and dynamic relations between hydrological processes, alteration, and inherited tectono-volcanic settings. Our findings suggest that the aquifer position and its thickness are strongly related to the behavior of the eruptive activity. By examining historical eruptions, we found that magmatic intrusions are likely to generate a phreatomagmatic eruption where a wide aquifer is located within the first ~300 m below the ground surface.

At greater depths, an elongated clay cap (0–2 km bsl) seems to efficiently seal a deep gas-rich reservoir (2–4.5 km bsl) from shallow water-rich regions, except beneath the 2000 A.D. caldera. In this area, hot magmatic gases ascend toward the surface within a ~1.2 km-long permeable conduit, inducing steam explosions in the liquid-dominated surrounding. We propose that this energetic phase change explains the long-period seismicity, and reveals the mixing mechanism responsible for the increase of water content observed in the fumarolic composition after the 2000 A.D. eruption.

The present study introduces a relevant multidisciplinary approach to better image and understand volcanic edifices. We believe this work can help to enhance monitoring strategies on volcanoes, in order to further mitigate hazards associated with magmatic-hydrothermal interactions.

### Data Availability Statement

Datasets generated by this study (i.e., raw and processed magnetotellurics time-series, electrical resistivity model, hypocenters, thermal image, and self-potential measurements) are available on the Zenodo open-access repository operated by the CERN: <https://doi.org/10.5281/zenodo.4745262>.

### Acknowledgments

This research was supported by the Ministry of Education, Culture, Sports, Science, and Technology of Japan (MEXT) under the program “Integrated Program for Next Generations Volcano Research and Human Resource Development” (<http://www.kazan-pj.jp/>), by the Japan Society for the Promotion of Science (JSPS) for postdoctoral fellowship P19316 (M.Gresse.), and the Grant-in-Aid for JSPS fellows 19F19316 (M.Gresse).

The magnetotellurics and self-potential data acquisition were supported by the MEXT under the program “Multidisciplinary Research Project for High Strain Rate Zones” during 2008–2013, and were acquired under the supervision of the Japan Meteorological Agency. Staffs of the technical supporting section for observational research in the Earthquake Research Institute, the University of Tokyo: C. Fujita, T. Nakajima, M. Masuda, K. Miyakawa, T. Mori, and A. Watanabe were acknowledged for their assistance during the magnetotellurics data acquisition in the Miyakejima Island. We also thank Miyakejima landowners and village offices for permitting us to conduct the observations. Most computations presented in this paper were performed using the computer systems of the Earthquake Information Center at the Earthquake Research Institute. We thank W. Siripunvaraporn for letting us use his 3-D inversion code. The authors also thank A. Chave for providing his magnetotelluric data processing program (BIRRP, <https://www.whoiepi.edu/science/AOPE/people/achave/Site/Next1.html>, last accessed in May 2021). Miyakejima meteorological data used in this work were collected by the Japan Meteorological Agency on the following website (in Japanese, last accessed in May 2021: [http://www.data.jma.go.jp/obd/stats/etrn/view/annually\\_s.php?prec\\_no=44&block\\_no=47677&year=2012&month=1&day=&view](http://www.data.jma.go.jp/obd/stats/etrn/view/annually_s.php?prec_no=44&block_no=47677&year=2012&month=1&day=&view)). The authors are grateful to Volker Rath and one anonymous reviewer for their valuable comments and suggestions that helped to improve and clarify the text. We also thank Ryuichi Nishiyama, Yuji Itoh, Pascal Saille, Philippe Labazuy, and Niklas Linde for their helpful discussions.

### References

Aizawa, K. (2004). A large self-potential anomaly and its changes on the quiet Mt. Fuji, Japan. *Geophysical Research Letters*, 31(5). <https://doi.org/10.1029/2004GL019462>

Aizawa, K., Ogawa, Y., & Ishido, T. (2009). Groundwater flow and hydrothermal systems within volcanic edifices: Delineation by electric self-potential and magnetotellurics. *Journal of Geophysical Research: Solid Earth*, 114(B1), B01208. <https://doi.org/10.1029/2008JB005910>

Aizawa, K., Yoshimura, R., & Oshiman, N. (2004). Splitting of the Philippine Sea Plate and a magma chamber beneath Mt. Fuji. *Geophysical Research Letters*, 31(9). <https://doi.org/10.1029/2004GL019477>

Aizawa, K., Yoshimura, R., Oshiman, N., Yamazaki, K., Uto, T., Ogawa, Y., et al. (2005). Hydrothermal system beneath Mt. Fuji volcano inferred from magnetotellurics and electric self-potential. *Earth and Planetary Science Letters*, 235(1–2), 343–355. <https://doi.org/10.1016/j.epsl.2005.03.023>

Amma-Miyasaka, M., & Nakagawa, M. (2003). Evolution of deeper basaltic and shallower andesitic magmas during the AD 1469–1983 eruptions of Miyake-Jima Volcano, Izu–Mariana Arc: Inferences from temporal variations of mineral compositions in crystal-clots. *Journal of Petrology*, 44(12), 2113–2138. <https://doi.org/10.1093/petrology/egg072>

Amma-Miyasaka, M., Nakagawa, M., & Nakada, S. (2005). Magma plumbing system of the 2000 eruption of Miyakejima Volcano, Japan. *Bulletin of Volcanology*, 67(3), 254–267. <https://doi.org/10.1007/s00445-004-0408-0>

Aoki, S., Shindo, S., & Chihara, K. (1984). Groundwater of the Miyakejima Volcanic Island in the Izu Volcanic Chain, Japan, Second series bulletin of the Volcanological Society of Japan (Vol. 29, pp. S324–S334). TOKUBE. [https://doi.org/10.18940/kazanc.29.TOKUBE\\_S324](https://doi.org/10.18940/kazanc.29.TOKUBE_S324)

Arai, T. (1978). Water balance of lake Tairo in Miyakejima island. *Geographical Review of Japan*, 51(9), 704–720. <https://doi.org/10.4157/grj.51.704>

Arai, T., Mori, K., & Takayama, S. (1977). General characteristics of the inland water in Miyake Island. *Japanese Journal of Limnology (Rikusuigaku Zasshi)*, 38(1), 1–8. <https://doi.org/10.3739/rikusui.38.1>

Arnason, K., Eysteinsson, H., & Hersir, G. P. (2010). Joint 1D inversion of TEM and MT data and 3D inversion of MT data in the Hengill area, SW Iceland. *Geothermics*, 39(1), 13–34. <https://doi.org/10.1016/j.geothermics.2010.01.002>

Ball, J. L., Taron, J., Reid, M. E., Hurwitz, S., Finn, C., & Bedrosian, P. (2018). Combining multiphase groundwater flow and slope stability models to assess stratovolcano flank collapse in the cascade range. *Journal of Geophysical Research: Solid Earth*, 123(4), 2787–2805. <https://doi.org/10.1002/2017JB015156>

Bedrosian, P. A., Peacock, J. R., Bowles-Martinez, E., Schultz, A., & Hill, G. J. (2018). Crustal inheritance and a top-down control on arc magmatism at Mount St Helens. *Nature Geoscience*, 11(11), 865–870. <https://doi.org/10.1038/s41561-018-0217-2>

Bertrand, E. A., Caldwell, T. G., Hill, G. J., Bennie, S. L., & Soengkono, S. (2013). Magnetotelluric imaging of the Ohaaki geothermal system, New Zealand: Implications for locating basement permeability. *Journal of Volcanology and Geothermal Research*, 268, 36–45. <https://doi.org/10.1016/j.jvolgeores.2013.10.010>

Browne, P. R. L., & Lawless, J. V. (2001). Characteristics of hydrothermal eruptions, with examples from New Zealand and elsewhere. *Earth-Science Reviews*, 52(4), 299–331. [https://doi.org/10.1016/S0012-8252\(00\)00030-1](https://doi.org/10.1016/S0012-8252(00)00030-1)

Byrdina, S., Vandemeulebrouck, J., Cardellini, C., Legaz, A., Camerlynck, C., Chiodini, G., et al. (2014). Relations between electrical resistivity, carbon dioxide flux, and self-potential in the shallow hydrothermal system of Solfatara (Phlegrean Fields, Italy). *Journal of Volcanology and Geothermal Research*, 283, 172–182. <https://doi.org/10.1016/j.jvolgeores.2014.07.010>

Cabrera, M. C., & Custodio, E. (2004). Groundwater flow in a volcanic–sedimentary coastal aquifer: Telde area, Gran Canaria, Canary Islands, Spain. *Hydrogeology Journal*, 12(3), 305–320. <https://doi.org/10.1007/s10040-003-0316-y>

Caldwell, T. G., Bibby, H. M., & Brown, C. (2004). The magnetotelluric phase tensor. *Geophysical Journal International*, 158(2), 457–469. <https://doi.org/10.1111/j.1365-246X.2004.02281.x>

Carlson, T. N., & Ripley, D. A. (1997). On the relation between NDVI, fractional vegetation cover, and leaf area index. *Remote Sensing of Environment*, 62(3), 241–252. [https://doi.org/10.1016/S0034-4257\(97\)00104-1](https://doi.org/10.1016/S0034-4257(97)00104-1)

Chave, A. D., & Thomson, D. J. (2003). A bounded influence regression estimator based on the statistics of the hat matrix. *Journal of the Royal Statistical Society: Series C (Applied Statistics)*, 52(3), 307–322. <https://doi.org/10.1111/1467-9876.00406>

Chiodini, G., Paonita, A., Aiuppa, A., Costa, A., Caliro, S., De Martino, P., et al. (2016). Magmas near the critical degassing pressure drive volcanic unrest towards a critical state. *Nature Communications*, 7, 13712. <https://doi.org/10.1038/ncomms13712>

Cordell, D., Unsworth, M. J., & Díaz, D. (2018). Imaging the Laguna del Maule Volcanic Field, central Chile using magnetotellurics: Evidence for crustal melt regions laterally-offset from surface vents and lava flows. *Earth and Planetary Science Letters*, 488, 168–180. <https://doi.org/10.1016/j.epsl.2018.01.007>

Dozier, J. (1981). A method for satellite identification of surface temperature fields of subpixel resolution. *Remote Sensing of Environment*, 11, 221–229. [https://doi.org/10.1016/0034-4257\(81\)90021-3](https://doi.org/10.1016/0034-4257(81)90021-3)

Dumont, M., Peltier, A., Roblin, E., Reninger, P.-A., Barde-Cabusson, S., Finizola, A., & Ferrazzini, V. (2019). Imagery of internal structure and destabilization features of active volcano by 3D high resolution airborne electromagnetism. *Scientific Reports*, 9(1), 18280. <https://doi.org/10.1038/s41598-019-54415-4>

Finizola, A., Aubert, M., Revil, A., Schütze, C., & Sortino, F. (2009). Importance of structural history in the summit area of Stromboli during the 2002–2003 eruptive crisis inferred from temperature, soil CO<sub>2</sub>, self-potential, and electrical resistivity tomography. *Journal of Volcanology and Geothermal Research*, 183(3–4), 213–227. <https://doi.org/10.1016/j.jvolgeores.2009.04.002>

- Flóvenz, Ó. G., Spangenberg, E., Kulenkampff, J., Árnason, K., Karlsdóttir, R., & Huenges, E. (2005). The role of electrical conduction in geothermal exploration. Presented at the Proceedings World Geothermal Congress Antalya (Vol. 9). Turkey. Retrieved from [https://www.researchgate.net/publication/266531271\\_The\\_Role\\_of\\_Electrical\\_Interface\\_Conduction\\_in\\_Geothermal\\_Exploration](https://www.researchgate.net/publication/266531271_The_Role_of_Electrical_Interface_Conduction_in_Geothermal_Exploration) (last accessed in May 2021)
- Fournier, R. O. (2007). Hydrothermal systems and volcano geochemistry. In D. Dzurlin (Ed.), *Volcano Deformation: Geodetic Monitoring Techniques* (pp. 323–341). Springer Berlin Heidelberg. [https://doi.org/10.1007/978-3-540-49302-0\\_10](https://doi.org/10.1007/978-3-540-49302-0_10)
- Furuya, M., Okubo, S., Sun, W., Tanaka, Y., Oikawa, J., Watanabe, H., & Maekawa, T. (2003). Spatiotemporal gravity changes at Miyakejima Volcano, Japan: Caldera collapse, explosive eruptions and magma movement. *Journal of Geophysical Research: Solid Earth*, 108(B4). <https://doi.org/10.1029/2002JB001989>
- Gailler, L., Marti, A., & Lénat, J.-F. (2018). Complex structure of Piton de la Fournaise and its underlying lithosphere revealed by magnetotelluric 3D inversion. *Journal of Volcanology and Geothermal Research*, 356, 200–210. <https://doi.org/10.1016/j.jvolgeores.2018.03.006>
- Gasperikova, E., Rosenkjaer, G. K., Árnason, K., Newman, G. A., & Lindsey, N. J. (2015). Resistivity characterization of the Krafla and Hengill geothermal fields through 3D MT inverse modeling. *Geothermics*, 57, 246–257. <https://doi.org/10.1016/j.geothermics.2015.06.015>
- Geshi, N. (2009). Asymmetric growth of collapsed caldera by oblique subsidence during the 2000 eruption of Miyakejima, Japan. *Earth and Planetary Science Letters*, 280(1), 149–158. <https://doi.org/10.1016/j.epsl.2009.01.027>
- Geshi, N., Németh, K., Noguchi, R., & Oikawa, T. (2019). Shift from magmatic to phreatomagmatic explosions controlled by the lateral evolution of a feeder dike in the Suoana-Kazahaya eruption, Miyakejima Volcano, Japan. *Earth and Planetary Science Letters*, 511, 177–189. <https://doi.org/10.1016/j.epsl.2019.01.038>
- Geshi, N., & Oikawa, T. (2016). Orientation of the eruption fissures controlled by a shallow magma chamber in Miyakejima. *Frontiers in Earth Science*, 4, 99. <https://doi.org/10.3389/feart.2016.00099>
- Geshi, N., & Shinohara, H. (2010). Conduit magma process of Miyakejima volcano inferred from basaltic juvenile materials in the products of the small ash eruptions during the continuous degassing. *Bulletin of the Volcanological Society of Japan*, 55(6), 241–250. [https://doi.org/10.18940/kazan.55.6\\_241](https://doi.org/10.18940/kazan.55.6_241)
- Grasse, M., Vandemeulebrouck, J., Byrdina, S., Chiodini, G., Revil, A., Johnson, T. C., et al. (2017). 3-D electrical resistivity tomography of the Solfatara crater (Italy): implication for the multiphase flow structure of the shallow hydrothermal system. *Journal of Geophysical Research: Solid Earth*, 122(11), 8749–8768. <https://doi.org/10.1002/2017JB014389>
- Grobbe, N., & Barde-Cabusson, S. (2019). Self-potential studies in volcanic environments: A cheap and efficient method for multiscale fluid-flow investigations. *International Journal of Geophysics*, 2019, 985824. <https://doi.org/10.1155/2019/2985824>
- Harris, A. (2013). *Thermal Remote Sensing of Active Volcanoes: A User's Manual*. Cambridge University Press. <https://doi.org/10.1017/CBO9781139029346>
- Hata, M., Uyeshima, M., Handa, S., Shimoizumi, M., Tanaka, Y., et al. (2017). 3-D electrical resistivity structure based on geomagnetic transfer functions exploring the features of arc magmatism beneath Kyushu, Southwest Japan Arc. *Journal of Geophysical Research: Solid Earth*, 122(1), 172–190. <https://doi.org/10.1002/2016JB013179>
- Hata, M., Uyeshima, M., Tanaka, Y., Hashimoto, T., Oshiman, N., & Yoshimura, R. (2018). Three-dimensional electrical resistivity distribution beneath the Beppu–Shimabara graben with a focus on Aso Caldera, Southwest Japan subduction zone. *Journal of Geophysical Research: Solid Earth*, 123(8), 6397–6410. <https://doi.org/10.1029/2018JB015506>
- Hedenquist, J. W., & Henley, R. W. (1985). Hydrothermal eruptions in the Waitapu geothermal system, New Zealand: Their origin, associated breccias, and relation to precious metal mineralization. *Economic Geology*, 80(6), 1640–1668. <https://doi.org/10.2113/gsecongeo.80.6.1640>
- Heiken, G., & Wohletz, K. (1987). Tephra deposits associated with silicic domes and lava flows. *Geological Society of America Bulletin*, 212, 55–76. <https://doi.org/10.1130/SPE212-p55>
- Heise, W., Caldwell, T. G., Bertrand, E. A., Hill, G. J., Bennie, S. L., & Palmer, N. G. (2016). Imaging the deep source of the Rotorua and Waimangu geothermal fields, Taupo Volcanic Zone, New Zealand. *Journal of Volcanology and Geothermal Research*, 314, 39–48. <https://doi.org/10.1016/j.jvolgeores.2015.10.017>
- Hernández, P. A., Salazar, J. M., Shimoike, Y., Mori, T., Notsu, K., & Pérez, N. (2001). Diffuse emission of CO<sub>2</sub> from Miyakejima volcano, Japan. *Chemical Geology*, 177(1), 175–185. [https://doi.org/10.1016/S0009-2541\(00\)00390-9](https://doi.org/10.1016/S0009-2541(00)00390-9)
- Hersir, G. P., Árnason, K., Vilhjálmsson, A. M., Saemundsson, K., Ágústssdóttir, P., & Friðleifsson, G. Ó. (2020). Krýsuvík high temperature geothermal area in SW Iceland: Geological setting and 3D inversion of magnetotelluric (MT) resistivity data. *Journal of Volcanology and Geothermal Research*, 391, 106500. <https://doi.org/10.1016/j.jvolgeores.2018.11.021>
- Hill, G. J., Bibby, H. M., Ogawa, Y., Wallin, E. L., Bennie, S. L., Caldwell, T. G., et al. (2015). Structure of the Tongariro Volcanic system: Insights from magnetotelluric imaging. *Earth and Planetary Science Letters*, 432, 115–125. <https://doi.org/10.1016/j.epsl.2015.10.003>
- Hill, G. J., Caldwell, T. G., Heise, W., Chertkoff, D. G., Bibby, H. M., Burgess, M. K., et al. (2009). Distribution of melt beneath Mount St Helens and Mount Adams inferred from magnetotelluric data. *Nature Geoscience*, 2(11), 785–789. <https://doi.org/10.1038/ngeo661>
- Hirata, N., & Matsu'ura, M. (1987). Maximum-likelihood estimation of hypocenter with origin time eliminated using nonlinear inversion technique. *Physics of the Earth and Planetary Interiors*, 47, 50–61. [https://doi.org/10.1016/0031-9201\(87\)90066-5](https://doi.org/10.1016/0031-9201(87)90066-5)
- Hogg, C., Kiyan, D., Rath, V., Byrdina, S., Vandemeulebrouck, J., Revil, A., et al. (2017). 3-D interpretation of short-period magnetotelluric data at Furnas Volcano, Azores Islands. *Geophysical Journal International*, 213(1), 371–386. <https://doi.org/10.1093/gji/ggx512>
- Hurwitz, S., Kipp, K. L., Ingebritsen, S. E., & Reid, M. E. (2003). Groundwater flow, heat transport, and water table position within volcanic edifices: Implications for volcanic processes in the Cascade Range. *Journal of Geophysical Research: Solid Earth*, 108(B12). <https://doi.org/10.1029/2003JB002565>
- Ingebritsen, S. E., Geiger, S., Hurwitz, S., & Driesner, T. (2010). Numerical simulation of magmatic hydrothermal systems. *Reviews of Geophysics*, 48(1), RG1002. <https://doi.org/10.1029/2009RG000287>
- Ishido, T. (2004). Electrokinetic mechanism for the “W”-shaped self-potential profile on volcanoes. *Geophysical Research Letters*, 31(15). <https://doi.org/10.1029/2004GL020409>
- Ito, K. (1993). Cutoff depth of seismicity and large earthquakes near active volcanoes in Japan. *Tectonophysics*, 217(1), 11–21. [https://doi.org/10.1016/0040-1951\(93\)90198-S](https://doi.org/10.1016/0040-1951(93)90198-S)
- Izquierdo, T. (2014). Conceptual hydrogeological model and aquifer system classification of a small volcanic island (La Gomera; Canary Islands). *Catena*, 114, 119–128. <https://doi.org/10.1016/j.catena.2013.11.006>
- Jackson, D. B., & Kauahikaua, J. (1987). Regional self-potential anomalies at Kilauea Volcano (Hawaii). In R. W. Decker, T. L. Wright, & P. H. Stauffer (Eds.), *Volcanism in Hawaii* (pp. 947–959). <https://doi.org/10.3133/pp1350>

- Join, J.-L., Folio, J.-L., & Robineau, B. (2005). Aquifers and groundwater within active shield volcanoes. Evolution of conceptual models in the Piton de la Fournaise volcano. *Journal of Volcanology and Geothermal Research*, *147*(1), 187–201. <https://doi.org/10.1016/j.jvolgeores.2005.03.013>
- Kanda, W., Utsugi, M., Takakura, S., & Inoue, H. (2019). Hydrothermal system of the active crater of Aso volcano (Japan) inferred from a three-dimensional resistivity structure model. *Earth, Planets and Space*, *71*(1), 37. <https://doi.org/10.1186/s40623-019-1017-7>
- Kaneko, T., Yasuda, A., Shimano, T., Nakada, S., Fujii, T., Kanazawa, T., et al. (2005). Submarine flank eruption preceding caldera subsidence during the 2000 eruption of Miyakejima Volcano, Japan. *Bulletin of Volcanology*, *67*(3), 243–253. <https://doi.org/10.1007/s00445-004-0407-1>
- Kazahaya, K., Shinohara, H., Uto, K., Odai, M., Nakahori, Y., Mori, H., et al. (2004). Gigantic SO<sub>2</sub> emission from Miyakejima volcano, Japan, caused by caldera collapse. *Geology*, *32*(5), 425–428. <https://doi.org/10.1130/G20399.1>
- Kikuchi, M., Yamanaka, Y., & Koketsu, K. (2001). Source process of the long-period seismic pulses associated with the 2000 eruption of Miyake-jima volcano, and its implications. *Journal of Geography (Chigaku Zasshi)*, *110*(2), 204–216. [https://doi.org/10.5026/jgeography.110.2\\_204](https://doi.org/10.5026/jgeography.110.2_204)
- Klumbach, S., & Keppler, H. (2020). Electrical conductivity of HCl-bearing aqueous fluids to 700 °C and 1 GPa. *Contributions to Mineralogy and Petrology*, *175*(12), 114. <https://doi.org/10.1007/s00410-020-01754-5>
- Kobayashi, T., Ohminato, T., Ida, Y., & Fujita, E. (2012). Intermittent inflations recorded by broadband seismometers prior to caldera formation at Miyake-jima volcano in 2000. *Earth and Planetary Science Letters*, *357*–358, 145–151. <https://doi.org/10.1016/j.epsl.2012.09.039>
- Kumagai, H., Ohminato, T., Nakano, M., Ooi, M., Kubo, A., Inoue, H., & Oikawa, J. (2001). Very-Long-Period Seismic Signals and Caldera Formation at Miyake Island, Japan. *Science*, *293*(5530), 687–690. <https://doi.org/10.1126/science.1062136>
- Kuwano, O., Yoshida, S., Nakatani, M., & Uyeshima, M. (2015). Origin of transient self-potential signals associated with very long period seismic pulses observed during the 2000 activity of Miyakejima volcano. *Journal of Geophysical Research: Solid Earth*, *120*(5), 3544–3565. <https://doi.org/10.1002/2014JB011740>
- Lee, B., Unsworth, M., Árnason, K., & Cordell, D. (2020). Imaging the magmatic system beneath the Krafla geothermal field, Iceland: A new 3-D electrical resistivity model from inversion of magnetotelluric data. *Geophysical Journal International*, *220*(1), 541–567. <https://doi.org/10.1093/gji/ggz427>
- Lévy, L., Gibert, B., Sigmundsson, F., Flóvenz, Ó., Hersir, G. P., Briole, P., & Pezard, P. A. (2018). The role of smectites in the electrical conductivity of active hydrothermal systems: Electrical properties of core samples from Krafla volcano, Iceland. *Geophysical Journal International*, *215*(3), 1558–1582. <https://doi.org/10.1093/gji/ggy342>
- López, D. L., & Williams, S. N. (1993). Catastrophic volcanic collapse: Relation to hydrothermal processes. *Science*, *260*(5115), 1794–1796. <https://doi.org/10.1126/science.260.5115.1794>
- Machida, I., & Lee, S.-H. (2008). Delayed impact of New Volcanic Ejecta on ground water quality. *Groundwater*, *46*(4), 532–537. <https://doi.org/10.1111/j.1745-6584.2008.00452.x>
- Mannen, K., Abe, Y., Daita, Y., Doke, R., Harada, M., Kikugawa, G., et al. (2021). Volcanic unrest at Hakone volcano after the 2015 phreatic eruption: reactivation of a ruptured hydrothermal system? *Earth, Planets and Space*, *73*(1), 80. <https://doi.org/10.1186/s40623-021-01387-3>
- Mannen, K., Tanada, T., Jomori, A., Akatsuka, T., Kikugawa, G., Fukazawa, Y., et al. (2019). Source constraints for the 2015 phreatic eruption of Hakone volcano, Japan, based on geological analysis and resistivity structure. *Earth, Planets and Space*, *71*(1), 135. <https://doi.org/10.1186/s40623-019-1116-5>
- Matoza, R. S., & Chouet, B. A. (2010). Subevents of long-period seismicity: Implications for hydrothermal dynamics during the 2004–2008 eruption of Mount St. Helens. *Journal of Geophysical Research: Solid Earth*, *115*(B12). <https://doi.org/10.1029/2010JB007839>
- Matsunaga, Y., Kanda, W., Takakura, S., Koyama, T., Saito, Z., Seki, K., et al. (2020). Magmatic hydrothermal system inferred from the resistivity structure of Kusatsu-Shirane Volcano. *Journal of Volcanology and Geothermal Research*, *390*, 106742. <https://doi.org/10.1016/j.jvolgeores.2019.106742>
- Matsushima, N. (2005). H<sub>2</sub>O emission rate by the volcanic plume during the 2000–2002 Miyakejima volcanic activity. *Geophysical Research Letters*, *32*(14). <https://doi.org/10.1029/2005GL023217>
- McNutt, S. R. (1996). Seismic monitoring and eruption forecasting of volcanoes: A review of the state-of-the-art and case histories. In R. Scarpa, & R. I. Tilling (Eds.), *Monitoring and Mitigation of Volcano Hazards* (pp. 99–146). Springer Berlin Heidelberg. [https://doi.org/10.1007/978-3-642-80087-0\\_3](https://doi.org/10.1007/978-3-642-80087-0_3)
- Minakami, T. (1974). Chapter 1 - Seismology of Volcanoes in Japan. In L. Civetta, P. Gasparini, G. Luongo, & A. Rapolla (Eds.), *Developments in Solid Earth Geophysics* (pp. 1–27). Elsevier. <https://doi.org/10.1016/B978-0-444-41141-9.50007-3>
- Minami, T., Utsugi, M., Utada, H., Kagiya, T., & Inoue, H. (2018). Temporal variation in the resistivity structure of the first Nakadake crater, Aso volcano, Japan, during the magmatic eruptions from November 2014 to May 2015, as inferred by the ACTIVE electromagnetic monitoring system. *Earth, Planets and Space*, *70*(1), 138. <https://doi.org/10.1186/s40623-018-0909-2>
- Morita, Y., & Ohminato, T. (2020). Recent seismic activities at Miyake-jima volcano, SVC45-28, Presented at the Oral presentation at Jp-GU-AGU Joint meeting. Retrieved from <https://confit.atlas.jp/guide/event/jpgu2020/subject/SVC45-28/detail>
- Munekane, H., Oikawa, J., & Kobayashi, T. (2016). Mechanisms of step-like tilt changes and very long period seismic signals during the 2000 Miyakejima eruption: Insights from kinematic GPS. *Journal of Geophysical Research: Solid Earth*, *121*(4), 2932–2946. <https://doi.org/10.1002/2016JB012795>
- Murase, M., Irwan, M., Kariya, S., Tabei, T., Okuda, T., Miyajima, R., et al. (2006). Time dependent model of magma intrusion in and around Miyake and Kozu Islands, Central Japan in June–August, 2000. *Journal of Volcanology and Geothermal Research*, *150*(1), 213–231. <https://doi.org/10.1016/j.jvolgeores.2005.02.005>
- Nakada, S., Nagai, M., Kaneko, T., Nozawa, A., & Suzuki-Kamata, K. (2005). Chronology and products of the 2000 eruption of Miyakejima Volcano, Japan. *Bulletin of Volcanology*, *67*(3), 205–218. <https://doi.org/10.1007/s00445-004-0404-4>
- Nishida, Y., Matsushima, N., Goto, A., Nakayama, Y., Oyamada, A., Utsugi, M., & Oshima, H. (1996). Self-potential studies in volcanic areas (3) Miyake-jima, Esan and Usu. *Journal of the Faculty of Sciences, Hokkaido University*, *10*, 63–77. <https://doi.org/10.1080/09507119609549084>
- Nishimura, T., Murakami, M., Ozawa, S., Ishimoto, M., Sagiya, T., Yarai, H., & Ukawa, M. (2002). *Crustal deformation and source estimation before and after the 2000 Miyakejima eruption: Inflation and deflation sources from the 1983 eruption to May 2001* *Bulletin of the Earthquake* (Vol. 77, pp. 55–65). Research Institute, University of Tokyo. Retrieved from [https://repository.dl.itc.u-tokyo.ac.jp/?action=repository\\_uri&item\\_id=32595](https://repository.dl.itc.u-tokyo.ac.jp/?action=repository_uri&item_id=32595)
- Nishimura, T., Ozawa, S., Murakami, M., Sagiya, T., Tada, T., Kaidzu, M., & Ukawa, M. (2001). Crustal deformation caused by magma migration in the northern Izu Islands, Japan. *Geophysical Research Letters*, *28*(19), 3745–3748. <https://doi.org/10.1029/2001GL013051>

- Nono, F., Gibert, B., Parat, F., Loggia, D., Cichy, S. B., & Violat, M. (2020). Electrical conductivity of Icelandic deep geothermal reservoirs up to supercritical conditions: Insight from laboratory experiments. *Journal of Volcanology and Geothermal Research*, 391, 106364. <https://doi.org/10.1016/j.jvolgeores.2018.04.021>
- Ogawa, Y., Ichiki, M., Kanda, W., Mishina, M., & Asamori, K. (2014). Three-dimensional magnetotelluric imaging of crustal fluids and seismicity around Naruko volcano, NE Japan. *Earth, Planets and Space*, 66(1), 158. <https://doi.org/10.1186/s40623-014-0158-y>
- Ohminato, T. (2006). Characteristics and source modeling of broadband seismic signals associated with the hydrothermal system at Satsuma-Iwojima volcano, Japan. *Journal of Volcanology and Geothermal Research*, 158(3), 467–490. <https://doi.org/10.1016/j.jvolgeores.2006.08.004>
- Ozawa, T., & Ueda, H. (2011). Advanced interferometric synthetic aperture radar (InSAR) time series analysis using interferograms of multiple-orbit tracks: A case study on Miyake-jima. *Journal of Geophysical Research: Solid Earth*, 116(B12). <https://doi.org/10.1029/2011JB008489>
- Özgüç, A., Ataç, T., & Rybák, J. (2003). Temporal variability of the flare index (1966–2001). *Solar Physics*, 214(2), 375–396. <https://doi.org/10.1023/A:1024225802080>
- Parkinson, W. D. (1962). The influence of continents and oceans on geomagnetic variations. *Geophysical Journal International*, 6(4), 441–449. <https://doi.org/10.1111/j.1365-246X.1962.tb02992.x>
- Peacock, J. R., Mangan, M. T., McPhee, D., & Wannamaker, P. E. (2016). Three-dimensional electrical resistivity model of the hydrothermal system in Long Valley Caldera, California, from magnetotellurics. *Geophysical Research Letters*, 43(15), 7953–7962. <https://doi.org/10.1002/2016GL069263>
- Petrillo, Z., D'Auria, L., Mangiacapra, A., Chiodini, G., Caliro, S., & Scippaccola, S. (2019). A perturbative approach for modeling short-term fluid-driven ground deformation episodes on volcanoes: A case study in the Campi Flegrei Caldera (Italy). *Journal of Geophysical Research: Solid Earth*, 124(1), 1036–1056. <https://doi.org/10.1029/2018JB015844>
- Piña-Varas, P., Ledo, J., Queralt, P., Marcuello, A., Bellmunt, F., Hidalgo, R., & Messeiller, M. (2014). 3-D magnetotelluric exploration of Tenerife Geothermal System (Canary Islands, Spain). *Surveys in Geophysics*, 35(4), 1045–1064. <https://doi.org/10.1007/s10712-014-9280-4>
- Piña-Varas, P., Ledo, J., Queralt, P., Marcuello, A., Bellmunt, F., Ogaya, X., et al. (2015). Vertical collapse origin of Las Cañadas caldera (Tenerife, Canary Islands) revealed by 3-D magnetotelluric inversion. *Geophysical Research Letters*, 42(6), 1710–1716. <https://doi.org/10.1002/2015GL063042>
- Piña-Varas, P., Ledo, J., Queralt, P., Marcuello, A., & Perez, N. (2018). On the detectability of Teide volcano magma chambers (Tenerife, Canary Islands) with magnetotelluric data. *Earth, Planets and Space*, 70(1), 14. <https://doi.org/10.1186/s40623-018-0783-y>
- Pirajno, F. (2008). *Hydrothermal processes and mineral systems* (p. 1250). Springer.
- Planck, M. (1900). Entropie und Temperatur strahlender Wärme. *Annals of Physics*, 306(4), 719–737. <https://doi.org/10.1002/andp.19003060410>
- Pryet, A., d'Ozouville, N., Violette, S., Deffontaines, B., & Auken, E. (2012). Hydrogeological settings of a volcanic island (San Cristóbal, Galapagos) from joint interpretation of airborne electromagnetics and geomorphological observations. *hydrological Earth System and Sciences*, 16(12), 4571–4579. <https://doi.org/10.5194/hess-16-4571-2012>
- Qian, J.-H. (2008). Why precipitation is mostly concentrated over islands in the maritime continent. *Journal of the Atmospheric Sciences*, 65(4), 1428–1441. <https://doi.org/10.1175/2007JAS2422.1>
- Quist, A. S., & Marshall, W. L. (1968). Electrical conductances of aqueous sodium chloride solutions from 0 to 800 degree and at pressures to 4000 bars. *The Journal of Physical Chemistry*, 72(2), 684–703. <https://doi.org/10.1021/j100848a050>
- Reid, M. E. (2004). Massive collapse of volcano edifices triggered by hydrothermal pressurization. *Geology*, 32(5), 373–376. <https://doi.org/10.1130/G20300.1>
- Revil, A., Finizola, A., Piscitelli, S., Rizzo, E., Ricci, T., Crespy, A., et al. (2008). Inner structure of La Fossa di Vulcano (Vulcano Island, southern Tyrrhenian Sea, Italy) revealed by high-resolution electric resistivity tomography coupled with self-potential, temperature, and CO<sub>2</sub> diffuse degassing measurements. *Journal of Geophysical Research: Solid Earth*, 113(B7). <https://doi.org/10.1029/2007JB005394>
- Revil, A., Finizola, A., Ricci, T., Delcher, E., Peltier, A., Barde-Cabusson, S., et al. (2011). Hydrogeology of Stromboli volcano, Aeolian Islands (Italy) from the interpretation of resistivity tomograms, self-potential, soil temperature and soil CO<sub>2</sub> concentration measurements. *Geophysical Journal International*, 186(3), 1078–1094. <https://doi.org/10.1111/j.1365-246X.2011.05112.x>
- Revil, A., & Jardani, A. (2013). *The self-potential method: Theory and applications in environmental geosciences*. Cambridge University Press. <https://doi.org/10.1017/CBO9781139094252>
- Revil, A., Johnson, T. C., & Finizola, A. (2010). Three-dimensional resistivity tomography of Vulcan's forge, Vulcano Island, southern Italy. *Geophysical Research Letters*, 37(15). <https://doi.org/10.1029/2010GL043983>
- Revil, A., Qi, Y., Ghorbani, A., Coperey, A., Ahmed, A. S., Finizola, A., & Ricci, T. (2019). Induced polarization of volcanic rocks. 3. Imaging clay cap properties in geothermal fields. *Geophysical Journal International*, 218(2), 1398–1427. <https://doi.org/10.1093/gji/ggz207>
- Roberts, J. J., Duba, A. G., Bonner, B. P., & Kasameyer, P. W. (2001). The effects of capillarity on electrical resistivity during boiling in metashale from scientific corehole SB-15-D, The Geysers, California, USA. *Geothermics*, 30(2-3), 235–254. [https://doi.org/10.1016/S0375-6505\(00\)00052-3](https://doi.org/10.1016/S0375-6505(00)00052-3)
- Rosas-Carbajal, M., Komorowski, J.-C., Nicollin, F., & Gibert, D. (2016). Volcano electrical tomography unveils edifice collapse hazard linked to hydrothermal system structure and dynamics. *Scientific Reports*, 6, 29899. <https://doi.org/10.1038/srep29899>
- Saito, G., Morishita, Y., & Shinohara, H. (2010). Magma plumbing system of the 2000 eruption of Miyakejima volcano, Japan, deduced from volatile and major component contents of olivine-hosted melt inclusions. *Journal of Geophysical Research: Solid Earth*, 115(B11). <https://doi.org/10.1029/2010JB007433>
- Saito, G., Uto, K., Kazahaya, K., Shinohara, H., Kawanabe, Y., & Satoh, H. (2005). Petrological characteristics and volatile content of magma from the 2000 eruption of Miyakejima Volcano, Japan. *Bulletin of Volcanology*, 67(3), 268–280. <https://doi.org/10.1007/s00445-004-0409-z>
- Samrock, F., Grayver, A. V., Eysteinnsson, H., & Saar, M. O. (2018). Magnetotelluric image of transcrustal magmatic system beneath the Tulu Moye geothermal prospect in the Ethiopian rift. *Geophysical Research Letters*, 45(23), 812–855. <https://doi.org/10.1029/2018GL080333>
- Sasai, Y., Uyeshima, M., Zlotnicki, J., Utada, H., Kagiya, T., Hashimoto, T., & Takahashi, Y. (2002). Magnetic and electric field observations during the 2000 activity of Miyake-jima volcano, Central Japan. *Earth and Planetary Science Letters*, 203(2), 769–777. [https://doi.org/10.1016/S0012-821X\(02\)00857-9](https://doi.org/10.1016/S0012-821X(02)00857-9)
- Sasai, Y., Zlotnicki, J., Nishida, Y., Yvetot, P., Morat, P., Murakami, H., et al. (1997). Electromagnetic monitoring of Miyake-jima Volcano, Izu-Bonn Arc, Japan: A preliminary report. *Journal of geomagnetism and geoelectricity*, 49(11-12), 1293–1316. <https://doi.org/10.5636/jgg.49.1293>

- Sato, T., Machida, I., Takahashi, M., & Nakamura, T. (2006). Geochemical changes in spring water associated with the 2000 eruption of the Miyakejima volcano, Japan. *pure and applied geophysics*, 163(4), 809–823. <https://doi.org/10.1007/s00024-006-0042-1>
- Schwalenberg, K., Rath, V., & Haak, V. (2002). Sensitivity studies applied to a two-dimensional resistivity model from the Central Andes. *Geophysical Journal International*, 150(3), 673–686. <https://doi.org/10.1046/j.1365-246X.2002.01734.x>
- Scott, S. W. (2020). Decompression boiling and natural steam cap formation in high-enthalpy geothermal systems. *Journal of Volcanology and Geothermal Research*, 395, 106765. <https://doi.org/10.1016/j.jvolgeores.2019.106765>
- Scott, S. W., Driesner, T., & Weis, P. (2015). Geologic controls on supercritical geothermal resources above magmatic intrusions. *Nature Communications*, 6(1), 7837. <https://doi.org/10.1038/ncomms8837>
- Shinohara, H., Geshi, N., Matsushima, N., Saito, G., & Kazahaya, R. (2017). Volcanic gas composition changes during the gradual decrease of the gigantic degassing activity of Miyakejima volcano, Japan, 2000–2015. *Bulletin of Volcanology*, 79(2), 21. <https://doi.org/10.1007/s00445-017-1105-0>
- Siebert, L., Glicken, H., & Ui, T. (1987). Volcanic hazards from Bezymianny - and Bandai-type eruptions. *Bulletin of Volcanology*, 49(1), 435–459. <https://doi.org/10.1007/BF01046635>
- Siripunvaraporn, W. (2012). Three-dimensional magnetotelluric inversion: An introductory guide for developers and users. *Surveys in Geophysics*, 33(1), 5–27. <https://doi.org/10.1007/s10712-011-9122-6>
- Siripunvaraporn, W., & Egbert, G. (2009). WSINV3DMT: Vertical magnetic field transfer function inversion and parallel implementation. *Physics of the Earth and Planetary Interiors*, 173(3–4), 317–329. <https://doi.org/10.1016/j.pepi.2009.01.013>
- Siripunvaraporn, W., G. Egbert, Y. Lenbury, and M. Uyeshima (2005), Three-dimensional magnetotelluric inversion: Data-space method, *Physics of the Earth and Planetary Interiors*, 150(1), 3–14. <https://doi.org/10.1016/j.pepi.2004.08.023>
- Sobrinho, J. A., Caselles, V., & Becker, F. (1990). Significance of the remotely sensed thermal infrared measurements obtained over a citrus orchard. *ISPRS Journal of Photogrammetry and Remote Sensing*, 44(6), 343–354. [https://doi.org/10.1016/0924-2716\(90\)90077-O](https://doi.org/10.1016/0924-2716(90)90077-O)
- Soyer, W., Mackie, R., Hallinan, S., Pavesi, A., Nordquist, G., Suminar, A., et al. (2018). Geologically consistent multiphysics imaging of the Darajat geothermal steam field. *First Break*, 36, 77–83. <https://doi.org/10.3997/1365-2397.n0102>
- Stix, J. (2018). Understanding fast and slow unrest at volcanoes and implications for eruption forecasting. *Frontiers in Earth Science*, 6, 56. <https://doi.org/10.3389/feart.2018.00056>
- Triahadini, A., Aizawa, K., Teguri, Y., Koyama, T., Tsukamoto, K., Muramatsu, D., et al. (2019). Magnetotelluric transect of Unzen graben, Japan: conductors associated with normal faults. *Earth, Planets and Space*, 71(1), 28. <https://doi.org/10.1186/s40623-019-1004-z>
- Tsukamoto, K., Aizawa, K., Chiba, K., Kanda, W., Uyeshima, M., Koyama, T., et al. (2018). Three-dimensional resistivity structure of Iwo-Yama volcano, Kirishima volcanic complex, Japan: Relationship to shallow seismicity, surface uplift, and a small phreatic eruption. *Geophysical Research Letters*, 45(23), 812–828. <https://doi.org/10.1029/2018GL080202>
- Tsukui, M., Kawanabe, Y., & Niihori, K. (2005). Geological Map of Miyake Jima Volcano Geological Map of Volcanoes (Vol. 12). Japan: Geological Survey of Japan, AIST. [https://gbank.gsj.jp/volcano/Act\\_Vol/miyakejima/index-e.html](https://gbank.gsj.jp/volcano/Act_Vol/miyakejima/index-e.html)
- Tsukui, M., Niihori, K., Kawanabe, Y., & Suzuki, Y. (2001). Stratigraphy and Formation of Miyakejima Volcano. *Journal of Geography (Chigaku Zasshi)*, 110(2), 156–167. [https://doi.org/10.5026/jgeography.110.2\\_156](https://doi.org/10.5026/jgeography.110.2_156)
- Tsukui, M., & Suzuki, Y. (1998). Eruptive history of Miyakejima volcano during the last 7000 years. *Bulletin of Volcanological Society of Japan*, 43(4), 149–166. [https://doi.org/10.18940/kazan.43.4\\_149](https://doi.org/10.18940/kazan.43.4_149)
- Tyler, R. H., Boyer, T. P., Minami, T., Zweng, M. M., & Reagan, J. R. (2017). Electrical conductivity of the global ocean. *Earth, Planets and Space*, 69(1), 156. <https://doi.org/10.1186/s40623-017-0739-7>
- Uchida, T. (2005). Three-dimensional magnetotelluric investigation in geothermal fields in Japan and Indonesia Proceedings World Geothermal Congress (Vol. 12). Antalya, Turkey. Retrieved from <https://www.geothermal-energy.org/pdf/IGAstandard/WGC/2005/0752.pdf>
- Ueda, H., Fujita, E., Ukawa, M., Yamamoto, E., Irwan, M., & Kimata, F. (2005). Magma intrusion and discharge process at the initial stage of the 2000 activity of Miyakejima, Central Japan, inferred from tilt and GPS data. *Geophysical Journal International*, 161(3), 891–906. <https://doi.org/10.1111/j.1365-246X.2005.02602.x>
- Ueki, S., Shimizu, H., Koyama, J., & Takagi, A. (1984). Seismic activity following the 1983 eruption of Miyakejimas. *Bulletin of the Volcanological Society of Japan*, 29, S68–S80. [https://doi.org/10.18940/kazanc.29.TOKUBE\\_S68](https://doi.org/10.18940/kazanc.29.TOKUBE_S68)
- Uehira, K., Baba, T., Mori, H., Katayama, H., & Hamada, N. (2005). Earthquake swarms preceding the 2000 eruption of Miyakejima volcano, Japan. *Bulletin of Volcanology*, 67(3), 219–230. <https://doi.org/10.1007/s00445-004-0405-3>
- Ushioda, M., Takahashi, E., Hamada, M., Suzuki, T., & Niihori, K. (2018). Evolution of magma plumbing system in Miyakejima volcano: Constraints from melting experiments. *Journal of Geophysical Research: Solid Earth*, 123(10), 8615–8636. <https://doi.org/10.1029/2018JB015910>
- Usui, Y., Ogawa, Y., Aizawa, K., Kanda, W., Hashimoto, T., Koyama, T., et al. (2016). Three-dimensional resistivity structure of Asama Volcano revealed by data-space magnetotelluric inversion using unstructured tetrahedral elements. *Geophysical Journal International*, 208(3), 1359–1372. <https://doi.org/10.1093/gji/ggw459>
- Violay, M., Gibert, B., Mainprice, D., Evans, B., Dautria, J.-M., Azais, P., & Pezard, P. (2012). An experimental study of the brittle-ductile transition of basalt at oceanic crust pressure and temperature conditions. *Journal of Geophysical Research: Solid Earth*, 117(B3). <https://doi.org/10.1029/2011JB008884>
- Waff, H. S., & Weill, D. F. (1975). Electrical conductivity of magmatic liquids: effects of temperature, oxygen fugacity and composition. *Earth and Planetary Science Letters*, 28(2), 254–260. [https://doi.org/10.1016/0012-821X\(75\)90235-6](https://doi.org/10.1016/0012-821X(75)90235-6)
- Walawender, J., M. Hajto, and P. Iwaniuk (2012), *A new ArcGIS toolset for automated mapping of land surface temperature with the use of LANDSAT satellite data*, 4371–4374. <https://doi.org/10.1109/IGARSS.2012.6350405>
- Waxman, M. H., & Smits, L. J. M. (1968). Electrical conductivities in oil-bearing shaly sands. *Society of Petroleum Engineers Journal*, 8(2), 107–122. <https://doi.org/10.2118/1863-A>
- Weis, P. (2015). The dynamic interplay between saline fluid flow and rock permeability in magmatic-hydrothermal systems. *Geofluids*, 15(1–2), 350–371. <https://doi.org/10.1111/gfl.12100>
- Yamaoka, K., Geshi, N., Hashimoto, T., Ingebritsen, S. E., & Oikawa, T. (2016). Special issue “The phreatic eruption of Mt. Ontake volcano in 2014”. *Earth, Planets and Space*, 68(1), 175. <https://doi.org/10.1186/s40623-016-0548-4>
- Yamaya, Y., Alanis, P. K. B., Takeuchi, A., Cordon, J. M., Mogi, T., Hashimoto, T., et al. (2013). A large hydrothermal reservoir beneath Taal Volcano (Philippines) revealed by magnetotelluric resistivity survey: 2D resistivity modeling. *Bulletin of Volcanology*, 75(7), 729. <https://doi.org/10.1007/s00445-013-0729-y>

- Yamaya, Y., Mogi, T., Honda, R., Hase, H., Hashimoto, T., & Uyeshima, M. (2017). Three-dimensional resistivity structure in Ishikari Lowland, Hokkaido, northeastern Japan—Implications to strain concentration mechanism. *Geochemistry, Geophysics, Geosystems*, 18(2), 735–754. <https://doi.org/10.1002/2016GC006771>
- Yasuda, A., Nakada, S., & Fujii, T. (2002). Composition of melt inclusions from 2000 Miyakejima eruption and implications for vigorous SO<sub>2</sub> emission (in Japanese with English abstract), (Vol. 77, pp. 43–54). Bulletin of the Earthquake Research Institute, University of Tokyo. Retrieved from [https://repository.dl.itc.u-tokyo.ac.jp/?action=repository\\_uri&item\\_id=32594](https://repository.dl.itc.u-tokyo.ac.jp/?action=repository_uri&item_id=32594)
- Yokoyama, T., Kobayashi, K., Kuritani, T., & Nakamura, E. (2003). Mantle metasomatism and rapid ascent of slab components beneath island arcs: Evidence from 238U-230Th-226Ra disequilibria of Miyakejima volcano, Izu arc, Japan. *Journal of Geophysical Research: Solid Earth*, 108(B7). <https://doi.org/10.1029/2002JB002103>
- Yoshimura, R., Ogawa, Y., Yukutake, Y., Kanda, W., Komori, S., Hase, H., et al. (2018). Resistivity characterisation of Hakone volcano, Central Japan, by three-dimensional magnetotelluric inversion. *Earth, Planets and Space*, 70(1), 66. <https://doi.org/10.1186/s40623-018-0848-y>
- Zlotnicki, J., Sasai, Y., Yvetot, P., Nishida, Y., Uyeshima, M., Fauquet, F., et al. (2003). Resistivity and self-potential changes associated with volcanic activity: The July 8, 2000 Miyake-jima eruption (Japan). *Earth and Planetary Science Letters*, 205(3–4), 139–154. [https://doi.org/10.1016/S0012-821X\(02\)01025-7](https://doi.org/10.1016/S0012-821X(02)01025-7)

## References From the Supporting Information

- Chen, J., Kuang, X., & Zheng, C. (2020). An empirical porosity–depth model for Earth’s crust. *Hydrogeology Journal*, 28, 2331–2339. <https://doi.org/10.1007/s10040-020-02214-x>
- Choi, D., Toda, H., & Kim, Y. (2014). Effect of sulfur dioxide (SO<sub>2</sub>) on growth and physiological activity in *Alnus sieboldiana* at Miyakejima Island in Japan. *Ecological Research*, 29(1), 103–110. <https://doi.org/10.1007/s11284-013-1103-4>
- Chouet, B. A., & Matoza, R. S. (2013). A multi-decadal view of seismic methods for detecting precursors of magma movement and eruption. *Journal of Volcanology and Geothermal Research*, 252, 108–175. <https://doi.org/10.1016/j.jvolgeores.2012.11.013>
- Finizola, A., Sortino, F., Lénat, J.-F., Aubert, M., Ripepe, M., & Valenza, M. (2003). The summit hydrothermal system of Stromboli. New insights from self-potential, temperature, CO<sub>2</sub> and fumarolic fluid measurements, with structural and monitoring implications. *Bulletin of Volcanology*, 65(7), 486–504. <https://doi.org/10.1007/s00445-003-0276-z>
- Frolova, J., Ladygin, V., & Rychagov, S. (2010). Petrophysical Alteration of Volcanic Rocks in Hydrothermal Systems of the Kuril - Kamchatka Island Arc. Presented at the Proceedings, World Geothermal Congress. Retrieved from [https://www.researchgate.net/publication/268266181\\_Petrophysical\\_Alteration\\_of\\_Volcanic\\_Rocks\\_in\\_Hydrothermal\\_Systems\\_of\\_the\\_Kuril-Kamchatka\\_Island\\_Arc](https://www.researchgate.net/publication/268266181_Petrophysical_Alteration_of_Volcanic_Rocks_in_Hydrothermal_Systems_of_the_Kuril-Kamchatka_Island_Arc)
- Honkura, Y. (1974). Electrical conductivity anomalies beneath the Japan Arc. *Journal of geomagnetism and geoelectricity*, 26(2), 147–171. <https://doi.org/10.5636/jgg.26.147>
- Jitsufuchi, T. (2010). *Surface temperature observations at Miyakejima by using the airborne radiative transfer spectral scanner (ARTS)* (p. 6). National Research Institute for Earth Science and Disaster Prevention (NEID). Retrieved from [https://www.data.jma.go.jp/svd/vois/data/tokyo/STOCK/kaisetsu/CCPVE/Report/106/kaiho\\_106\\_15.pdf](https://www.data.jma.go.jp/svd/vois/data/tokyo/STOCK/kaisetsu/CCPVE/Report/106/kaiho_106_15.pdf) (last accessed in May 2021).
- McNutt, S. R., & Roman, D. C. (2015). Chapter 59 - Volcanic Seismicity A2 - Sigurdsson, Haraldur, in *The Encyclopedia of Volcanoes* (2nd ed.), pp. 1011–1034, Academic Press. <https://doi.org/10.1016/B978-0-12-385938-9.00059-6>
- Nomura, Y., Kosugi, K. i., & Mizuyama, T. (2003). Physical properties of volcanic ash deposits in Miyakejima, Mt. Usu and Sakurajima. Analysis of physical properties of ash deposits in relation to mudflow occurrences. *Journal of Japan Society of Erosion*, 55(6), 3–12. [https://doi.org/10.11475/sabo1973.55.6\\_3](https://doi.org/10.11475/sabo1973.55.6_3)
- Revil, A., & Florsch, N. (2010). Determination of permeability from spectral induced polarization in granular media. *Geophysical Journal International*, 181(3), 1480–1498. <https://doi.org/10.1111/j.1365-246X.2010.04573.x>
- Revil, A., Le Breton, M., Niu, Q., Wallin, E., Haskins, E., & Thomas, D. M. (2017b). Induced polarization of volcanic rocks. 1. Surface versus quadrature conductivity. *Geophysical Journal International*, 208(2), 826–844. <https://doi.org/10.1093/gji/ggw444>
- Revil, A., Murugesu, M., Prasad, M., & Le Breton, M. (2017a). Alteration of volcanic rocks: A new non-intrusive indicator based on induced polarization measurements. *Journal of Volcanology and Geothermal Research*, 341, 351–362. <https://doi.org/10.1016/j.jvolgeores.2017.06.016>
- Revil, A., & Pezard, P. A. (1998). Streaming electrical potential anomaly along faults in geothermal areas. *Geophysical Research Letters*, 25(16), 3197–3200. <https://doi.org/10.1029/98GL02384>
- Tada, N., Tarits, P., Baba, K., Utada, H., Kasaya, T., & Suetsugu, D. (2016). Electromagnetic evidence for volatile-rich upwelling beneath the society hotspot, French Polynesia. *Geophysical Research Letters*, 43(23), 12021–12026. <https://doi.org/10.1002/2016GL071331>
- Taran, Y., Fischer, T. P., Pokrovsky, B., Sano, Y., Armienta, M. A., & Macias, J. L. (1998). Geochemistry of the volcano-hydrothermal system of El Chichón Volcano, Chiapas, Mexico. *Bulletin of Volcanology*, 59(6), 436–449. <https://doi.org/10.1007/s004450050202>
- Ussher, G., Harvey, C., Johnstone, R., & Anderson, E. (2000). Understanding the resistivities observed in geothermal systems. Proceedings World Geothermal Congress. Kyusyu-Tohoku, Japan, 1915-1920. Retrieved from <https://www.geothermal-energy.org/pdf/IGAstand-ard/WGC/2000/R0279.PDF>
- Villasante-Marcos, V., Finizola, A., Abella, R., Barde-Cabusson, S., Blanco, M. J., Brenes, B., et al. (2014). Hydrothermal system of Central Tenerife Volcanic Complex, Canary Islands (Spain), inferred from self-potential measurements. *Journal of Volcanology and Geothermal Research*, 272(0), 59–77. <https://doi.org/10.1016/j.jvolgeores.2013.12.007>